Electronic Supplementary Information for

Long-Range Exciton Transport in Brightly Fluorescent Furan/Phenylene Co-oligomer Crystals

Artur A. Mannanov,[a,b] Maxim S. Kazantsev,*[c,d] Anatoly D. Kuimov,[c,d] Vladislav G. Konstantinov,[b,e] Dmitry I. Dominskiy, [b,e] Vasiliy A. Trukhanov, [b,e] Daniil S. Anisimov, [b,e] Nikita V. Gultikov, [b] Vladimir V. Bruevich,[b,e] Igor P. Koskin,[c,d] Alina A. Sonina,[c,d] Tatyana V. Rybalova, [c,d] Inna K. Shundrina,[c,d] Evgeny A. Mostovich, [c,d] Dmitry Yu. Paraschuk,* [b,e] and Maxim S. Pshenichnikov*[a]

---

[a] *Optical Condensed Matter Physics Group, Zernike Institute for Advanced Materials, Rijksuniversiteit Groningen, Nijenborgh 4, Groningen 9747 AG, the Netherlands..*

[b] *Faculty of Physics & International Laser Center, Lomonosov Moscow State University, Leninskie Gory 1/62, Moscow 119991, Russia.*

[c] *N.N. Vorozhtsov Novosibirsk Institute of Organic Chemistry Lavrentieva 9, Novosibirsk, 630090, Russia.*

[d] *Novosibirsk State University, 630090, Pirogova 2, Novosibirsk, Russia*

[e] *Enikolopov Institute of Synthetic Polymeric Materials, Russian Academy of Science, Profsoyuznaya 70, Moscow 117393, Russia.*

**E-mail: maximkazantsev1988@gmail.com, paras@physics.msu.ru, m.s.pchenitchnikov@rug.nl*

Table of Contents

1. Experimental details of materials synthesis and characterization

All reagents and solvents were purchased from commercial sources (Sigma-Aldrich, Acros) and used without additional purification. Combustion analysis was performed by a CHN-analyzer (EURO EA). NMR spectra were recorded in a Bruker AV 400 spectrometer. Mass spectra were obtained in a Thermo Electron Corporation DFS mass spectrometer. IR spectra were recorded in the transmission mode in a Bruker Tensor 27 FT-IR spectrometer in potassium bromide pellets. Thermogravimetry and differential scanning calorimetry analyses were performed in helium atmosphere using a NETZSCH STA 409 instrument with a heating rate of 10°C/min.

Cyclic voltammetry measurements were performed by computer-controlled P-8nano potentiostat (Elins, Russia) in combination with three-electrode cell (Gamry); 0.1 M solution of tetrabytylammonium hexafluorophosphate in CH_3CN was used as supporting electrolyte. The Pt, Pt wire and Ag/AgCl were used as working, counter and reference electrodes, respectively. The reference electrode was calibrated by measuring the redox potential of ferrocene. The measurements were performed for the thin films on working electrode immersed into the CH_3CN solution. Multiple drop-casting of $CHCl_3$ solution of FP5 and FP8 compounds was used for thin film deposition. The HOMO energy levels were estimated using onset oxidation potentials according to equation:

$$E_{\mathrm{HOMO}} = -(E_{\mathrm{ox}}^{\mathrm{onset}} + 4.8) \text{ (eV)}$$

To grow 5,5'-bis(4-(5-phenylfuran-2-yl)phenyl)-2,2'-bifuran (FP8) crystals, we used PVT method at a temperature of ~430°C and a stream of 50 sccm. For the single-crystal X-ray analysis Bruker KAPPA APEX II diffractometer with graphite monochromated MoKa radiation was used. Integration and scaling of the intensity data were accomplished using SAINT.[1] Absorption corrections were applied using SADABS.[2] The structures were solved by direct methods using the SHELXS-97 software.[3] Refinement was carried out using the full-matrix least-squares technique using SHELXL.[3] All non-hydrogen atoms were refined anisotropically. Hydrogen atom positions were calculated geometrically and refined isotropically using the riding model. The asymmetric unit contains half a molecule because of molecular laying on the center of symmetry.

Crystallographic data for FP8 structure have been deposited at the Cambridge Crystallographic Data Centre as supplementary publication no. CCDC 1851983. Copy of the data can be obtained, free of charge, on application to CCDC, 12 Union Road, Cambridge CB21EZ, UK (fax: +44 122 3336033 or e-mail: deposit@ccdc.cam.ac.uk; internet: www.ccdc.cam.ac.uk).

2. Synthesis and characterization

For FP5 synthesis we used the previously described procedure[4] with only one stage vacuum sublimation. The possible self-dopant was identified by PL spectroscopy of raw FP5 in solution (Section 5). The structure of this dopant was inferred from the scheme of Suzuki cross-coupling reaction (Scheme S1), which could give a minor amount of FP8 as a byproduct.[5] We synthesized FP8 separately (Scheme S2) and confirmed its presence in raw FP5 powder by PL spectroscopy.

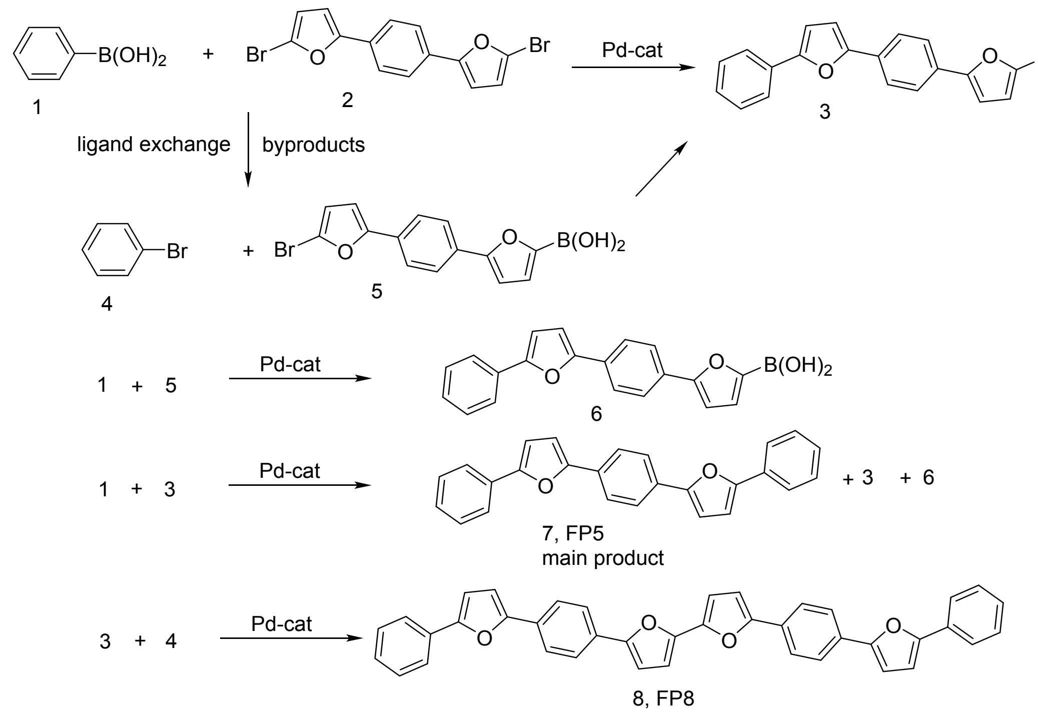

Scheme S1. Formation of presumed self-dopant FP8 *via* the Suzuki cross-coupling reaction of FP5 synthesis.

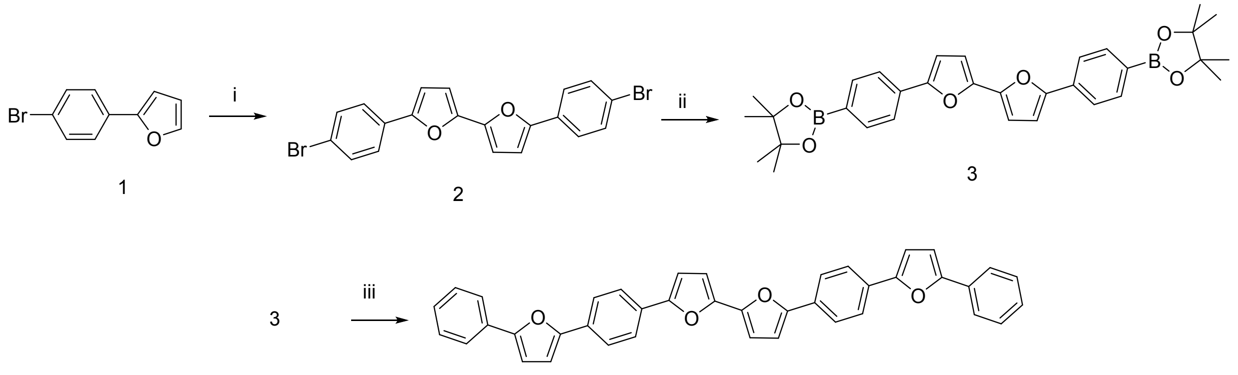

Scheme S2. Synthesis of FP8 (4). Reagents and conditions: i) $Pd(OAc)_2$ (50 mol%), O_2, DMSO, r.t., 70%; ii) bis(pinacolato)diboron, $Pd(dppf)_2Cl_2$ (10 mol%), KOAc, 1,4-dioxane, 100%; iii) 2-bromo-5-phenylfuran, $Pd(PPh_3)_4$ (10 mol%), $PhCH_3$-1M Na_2CO_3, 55%.

2.1. Synthesis of 5,5'-bis(4-bromophenyl)-2,2'-bifuran (2)

5,5'-bis(4-bromophenyl)-2,2'-bifuran was synthesized by optimized procedure reported in Ref.[6] Mixture of 2-(4-bromophenyl)furan **1** (0.68 g, 3.05 mmol), $Pd(OAc)_2$ (0.34 g, 0.50 mmol), CF_3COOH (0.23 mL, 3.05 mmol), DMSO (30 mL) was stirred 72 hr at r.t. under air flow in the dark. Obtained green-yellow precipitate was filtered off, washed carefully by water, methanol and dried at air. Yield 0.48 g (70%). Anal. calc. for $C_{20}H_{12}Br_2O_2$: C, 54.09; H, 2.72; Br, 35.98; found: C, 54.20; H, 2.66; Br, 35.66. ^{1}H NMR (400 MHz, $CDCl_3$) δ: 7.59 (d, ^3J=8.6 Hz, 4H), 7.53 (d, ^3J=8.6 Hz, 4H), 6.75 (d, ^3J=3.5 Hz, 2H), 6.72 (d, ^3J=3.5 Hz, 2H). HRMS(M^+): calc. for $C_{20}H_{12}Br_2O_2^{+\bullet}$: 441.9199, found: 441.9191.

2.2. Synthesis of 5,5'-bis(4-(4,4,5,5-tetramethyl-1,3,2-dioxaborolan-2-yl)phenyl)-2,2'-bifuran (3)

Mixture of 5,5'-bis(4-bromophenyl)-2,2'-bifuran **2** (0.40 g, 0.90 mmol), bis(pinacolato)diboron (0.69 g, 2.7 mmol), $Pd(dppf)_2Cl_2$ (0.066 g, 0.090 mmol), KOAc (0.530 g, 5.40 mmol), 1,4-dioxane (50 mL) were heated 24hr at 100°C under argon atmosphere. Solvent was removed by rotary *in vacuo*, obtained solid was washed by water to remove inorganic salts, dissolved in EtOAc and purified by flash-chromatography (SiO_2, hexane-EtOAc, 5:1). Yield 0.49 g (100%). Anal. calc. for $C_{32}H_{36}B_2O_6$: C, 71.41; H, 6.74; found: C, 71.20; H, 6.66. ^{1}H NMR (400 MHz, $CDCl_3$) δ: 7.51 (d, ^3J=7.4 Hz, 4H), 7.42 (d, ^3J=7.4 Hz, 4H), 6.58 (d, ^3J=3.6 Hz, 2H), 6.50 (d, ^3J=3.6 Hz, 2H), 1.05 (s, 12H), 0.95 (s, 12H). HRMS(M^+): calc. for $C_{32}H_{36}{}^{10}B_1{}^{11}B_1O_6^{+\bullet}$: 537.2728, found: 537.2731.

2.3. Synthesis of 5,5'-bis(4-(5-phenylfuran-2-yl)phenyl)-2,2'-bifuran (4).

Mixture of 5,5'-bis(4-(4,4,5,5-tetramethyl-1,3,2-dioxaborolan-2-yl)phenyl)-2,2'-bifuran **3** (0.45 g, 0.84 mmol), 2-bromo-5-phenylfuran (0.47 g, 2.10 mmol), $Pd(PPh_3)_4$ (0.098 g, 0.084 mmol) in toluene (50 mL) and 1M Na_2CO_3 (20 mL) were refluxed 72hr under argon atmosphere. Obtained green-yellow precipitate was filtered off, washed carefully by toluene, water, methanol and dried at air. Pure sample was obtained by physical vapor transport. Yield 0.26 g (55%). M.p.: 337°C. Anal. calc. for $C_{40}H_{26}O_4$: C, 84.19; H, 4.59; found: C, 83.90; H, 4.66. HRMS(M^+): calc. for $C_{40}H_{26}O_4^+$: 570.1826, found: 570.1831. ^{1}H NMR data was unable to obtain due to low solubility. X-ray single crystal analysis was used for the identification. The crystal system is monoclinic, $P2_1/c$, a=31.21(2), b=7.421(6), c=6.197(5) Å, β=92.23(4)°, V=1434(2) Å^3, Z=2, D_{calcd}=1.321g·cm^{-3}, μ(Mo-$K\alpha$) = 0.085mm^{-1}, F(000) = 596, (θ=3.04 – 25.02°, completeness=99.3%), T=296(2) K, light green plate, (1.4 × 0.53 × 0.02) mm^3, transmission 0.613 0. 862, 5103 measured reflections in index range -35<=h<=35, -8<=k<=8, -6<=l<=7, 2522 independent (R_{int}=0.1236), 199 parameters, R_1 = 0.1544 (for 1093 observed $I > 2\sigma(I)$, wR_2 = 0.4178 (all data), GOOF 1.182, largest diff. peak and hole 0.722 and - 0.516 e.A^{-3}. Unfortunately, we were unable to provide sufficient quantity of wR2 and high precision of C-C bond length due to low quality of FP8 crystals.

3. NMR, IR and HRMS spectra of synthesized compounds

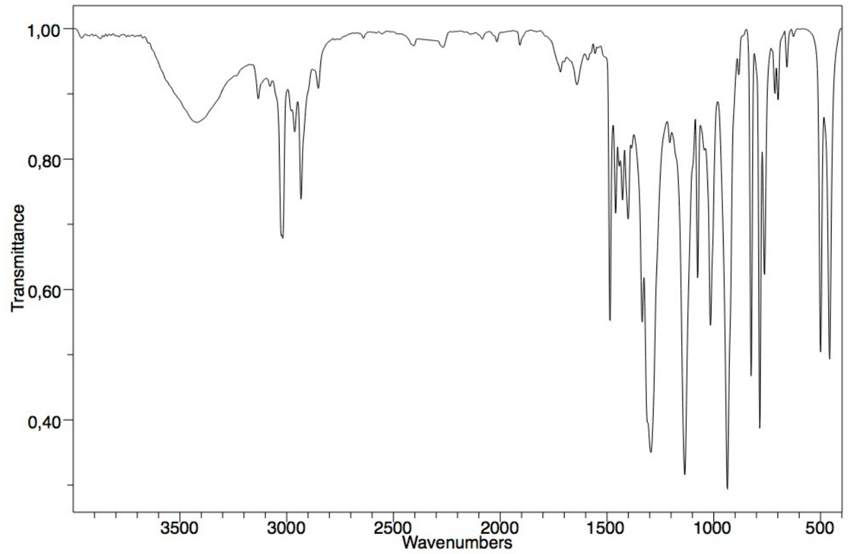

Figure S1. FT IR spectrum of 5,5'-bis(4-bromophenyl)-2,2'-bifuran (2) recorded in KBr.

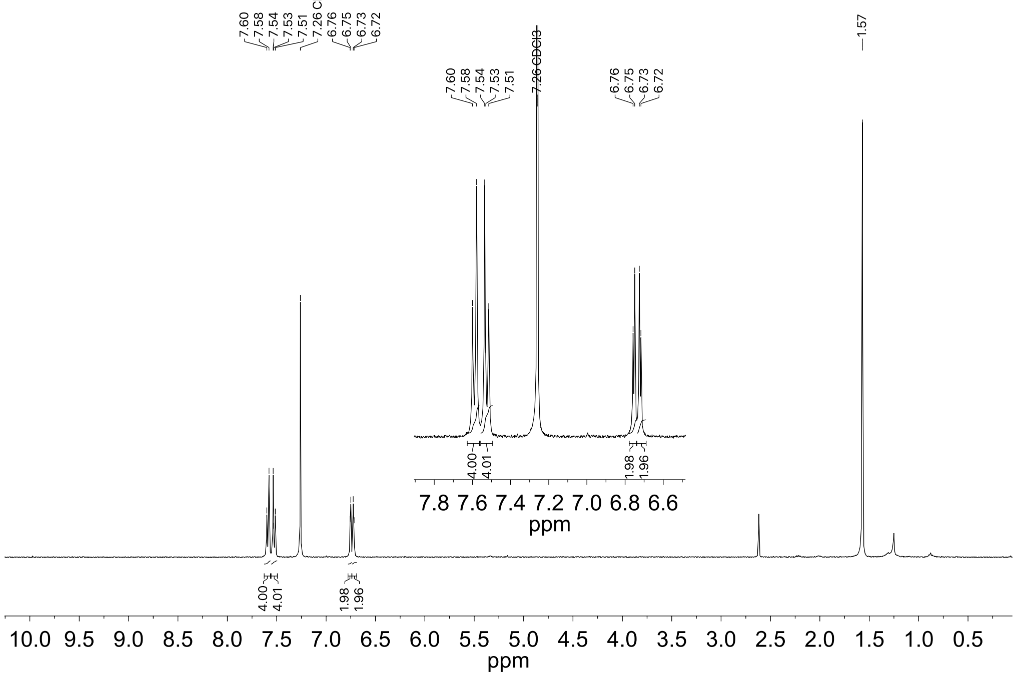

Figure S2. ^{1}H NMR spectrum of 5,5'-bis(4-bromophenyl)-2,2'-bifuran (**2**) recorded in $CDCl_3$.

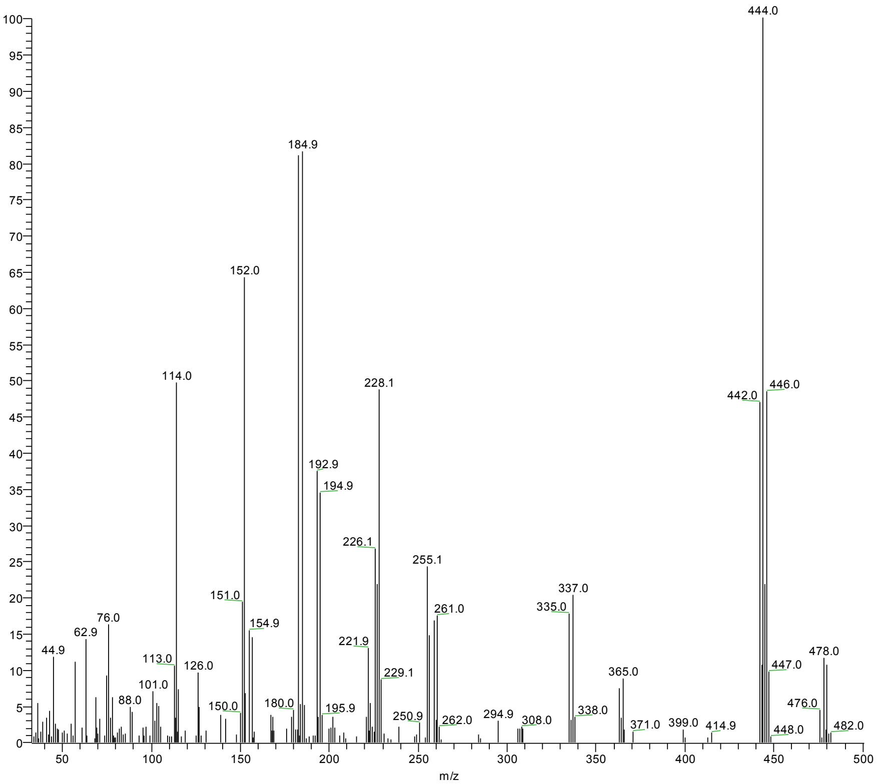

Figure S3. HMRS spectrum of 5,5'-bis(4-bromophenyl)-2,2'-bifuran (**2**).

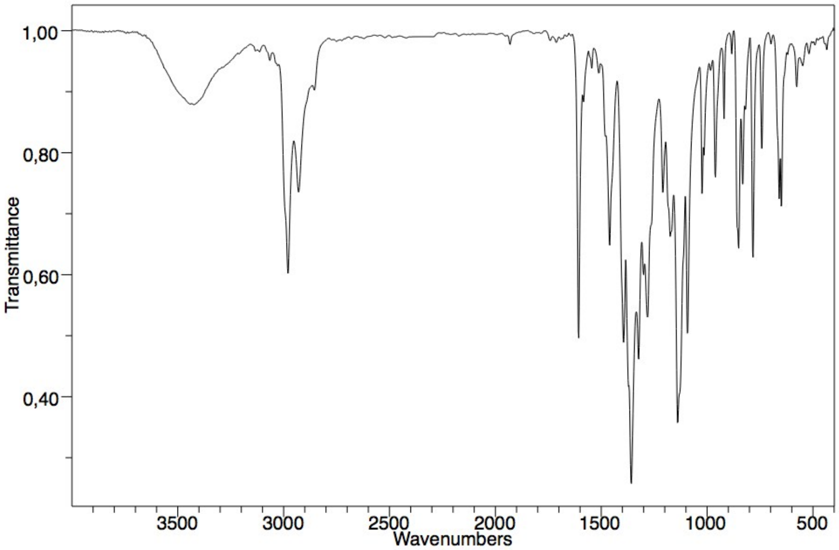

Figure S4. FTIR spectrum of 5,5'-bis(4-(4,4,5,5-tetramethyl-1,3,2-dioxaborolan-2-yl)phenyl)-2,2'-bifuran (**3**) recorded in KBr.

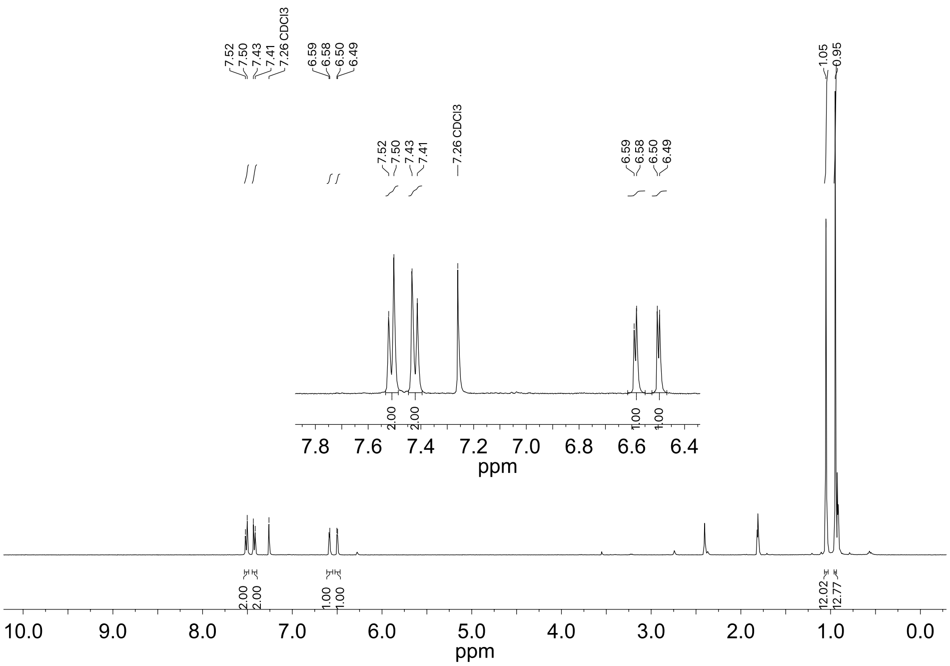

Figure S5. ^{1}H NMR spectrum of 5,5'-bis(4-(4,4,5,5-tetramethyl-1,3,2-dioxaborolan-2-yl)phenyl)-2,2'-bifuran (**3**) recorded in $CDCl_3$.

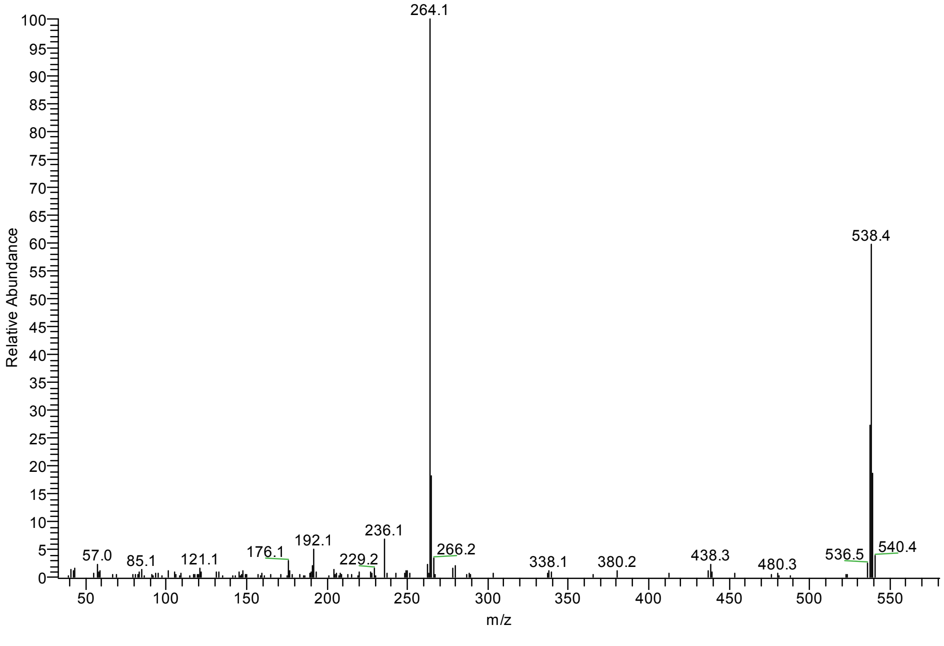

Figure S6. HMRS spectrum of 5,5'-bis(4-(4,4,5,5-tetramethyl-1,3,2-dioxaborolan-2-yl)phenyl)-2,2'-bifuran (**3**).

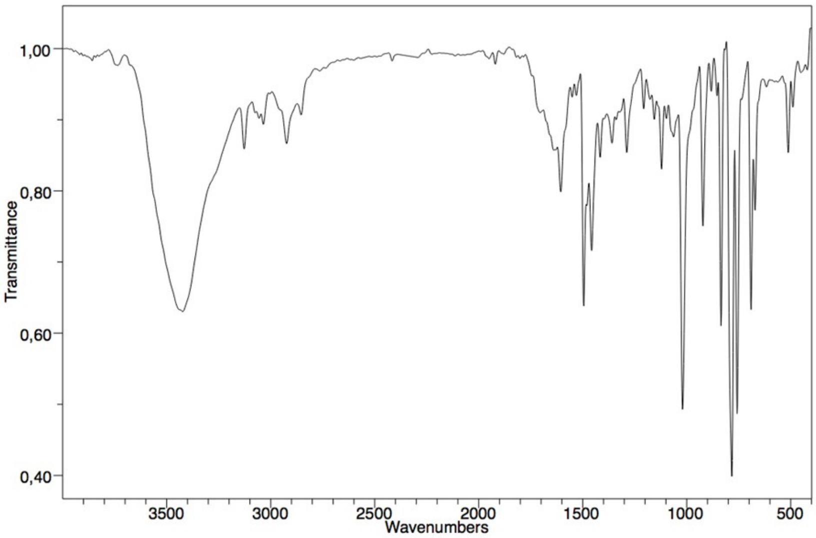

Figure S7. FTIR spectrum of 5,5'-bis(4-(5-phenylfuran-2-yl)phenyl)-2,2'-bifuran (**4, FP8**) recorded in KBr.

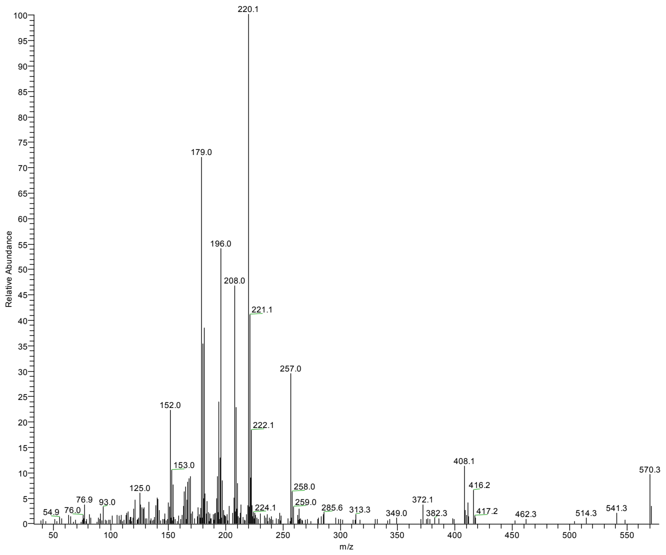

Figure S8. HMRS spectrum of 5,5'-bis(4-(5-phenylfuran-2-yl)phenyl)-2,2'-bifuran (**4, FP8**).

4. Förster radius calculations

The FP8 (quencher) extinction coefficient could not have been accurately measured in the doped FP5 single crystals due to their high background absorption (see SI Section 7, Figure S12). Therefore, the Förster radius for the donor (FP5, host) and acceptor (FP8, quencher) was estimated for two isolated molecules, i.e. their optical spectra and PL QY were taken from diluted solutions.

The donor PL spectrum, $F_D(\tilde{\nu})$, and the acceptor extinction spectrum, $\varepsilon_A(\tilde{\nu})$, measured in THF solutions are shown in Figure 1b. The former was normalized in such a way that the integral of PL spectrum equals to unity considering wavelengths in centimeters to enable its usage for Förster radius calculation:[7]

$$R_0{}^6 = \frac{9000 \cdot ln10 \cdot \gamma^2 \cdot QY_h}{128 \cdot \pi^5 \cdot n^4 \cdot N_A} \int_{\tilde{\nu}} \frac{\varepsilon_A(\tilde{\nu}) \cdot F_D(\tilde{\nu}) \cdot d(\tilde{\nu})}{\tilde{\nu}^4} \tag{S1}$$

where $QY_h = 91\%$ is PL QY of the donor molecule diluted in acetonitrile solvent[4]; N_A is Avogadro's constant; $\gamma^2 \approx 1.5$ is the orientational factor (see Section 12); n is the refractive index of a medium was taken as 2. The resulted Förster radius amounts to 4.9±0.5 nm.

5. Optical spectra of FP8, raw and purified FP5

Figure S9 presents optical spectra of FP8 in diluted solution.

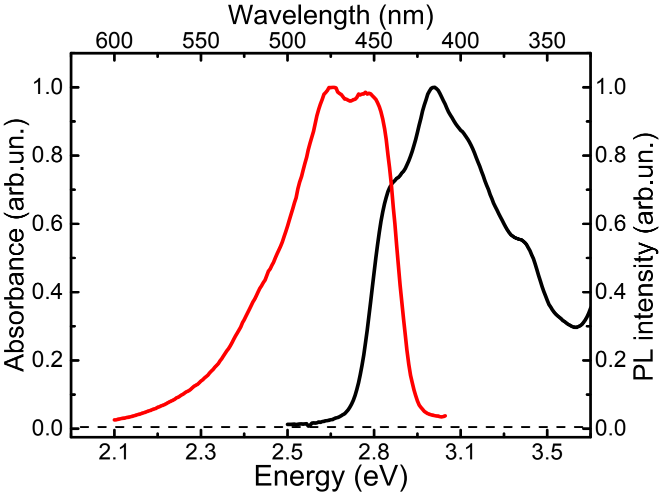

Figure S9. Absorption (black) and PL (red) spectra of FP8 in 10^{-6} M CH_2Cl_2 solution, the excitation wavelength was 405 nm.

To demonstrate that the FP5 material contains a small amount of FP8 as a synthetic by-product, we used the raw FP5 powder, recorded its optical spectra in solution and compared with those of FP8 (Figure S9a). The PL spectrum of raw FP5 solution recorded at an excitation wavelength of 460 nm corresponds to that of FP8. Therefore, we concluded that raw FP5 does contain minor amounts of FP8 as a synthetic by-product. PVT purification of the raw FP5 allowed us to reduce dramatically the content of FP8 as illustrated in Figure S9b.

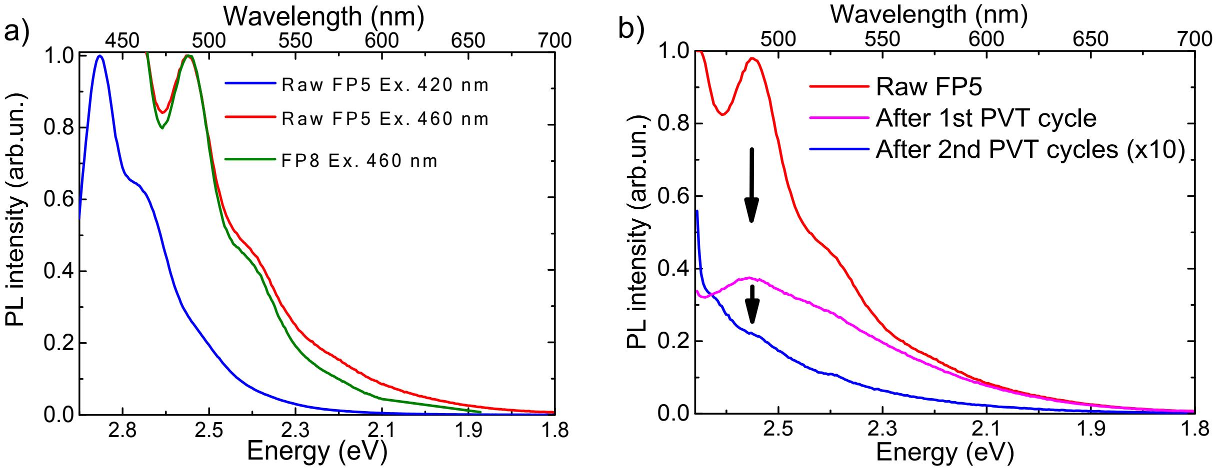

Figure S10. PL spectra of FP5 and FP8 samples dissolved in CH_2Cl_2(10^{-3}M). a) Raw FP5 at the excitation wavelengths of 420 nm (blue) and 460 nm (red); FP8 at the excitation wavelength of 460 nm (olive). b) FP5 samples at different purification stages: a raw sample (red); one-stage purified by PVT (magenta); doubly purified by PVT (blue, multiplied by a factor of 10). The excitation wavelength was chosen as 460 nm to provide the maximum contrast between the FP8 and FP5 spectra.

6. Microscope images of FP5 single crystals

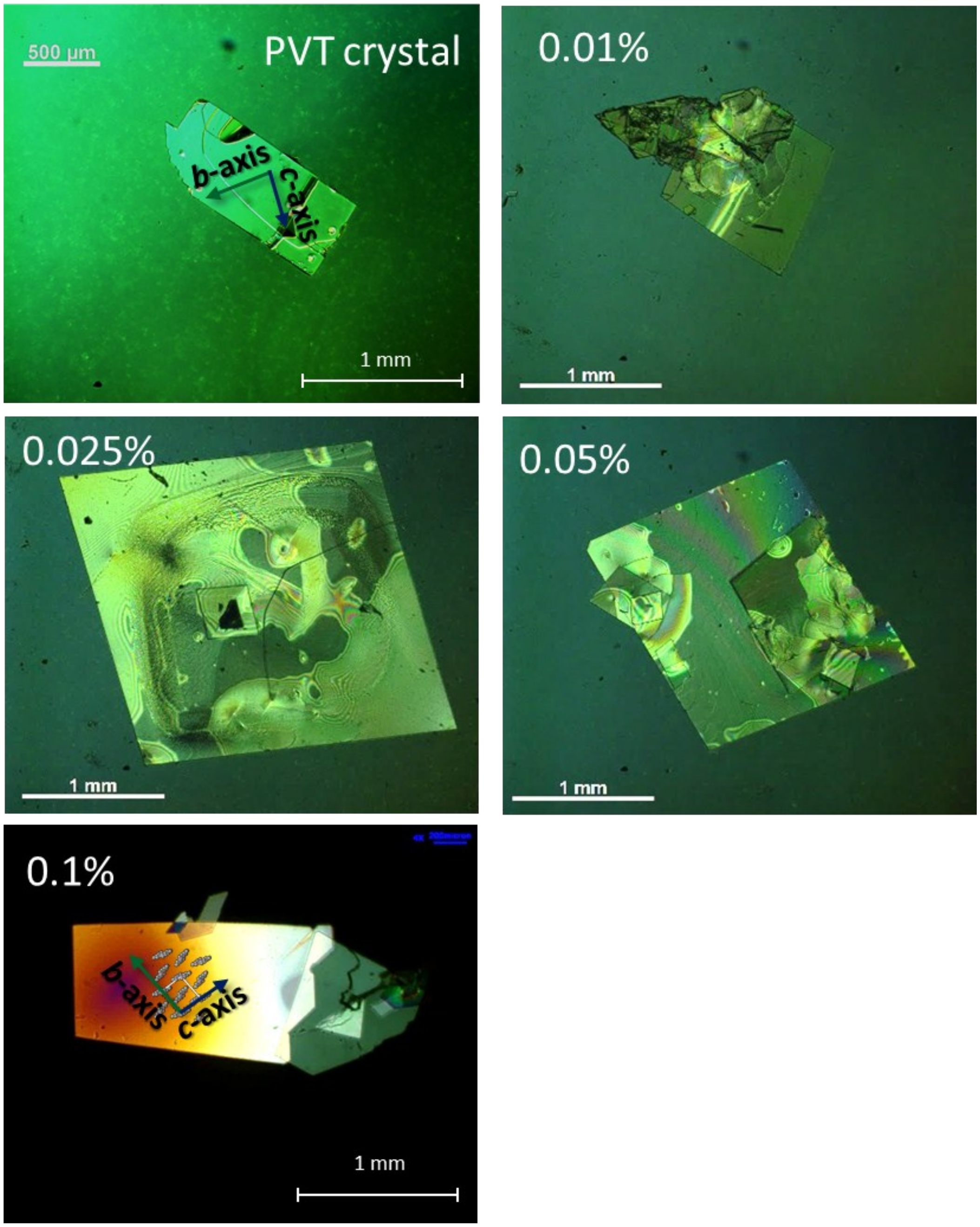

Figure S11. Microscopy images of the vapor-grown (PVT) and variously doped solution-grown FP5 single crystals. The prescribed doping levels for solution-grown crystal are indicated in the images. The crystallographic axes (*b-,c-*) orientations with respect to the crystal orientation are shown as green and blue arrows for the PVT and 0.1% doped crystals, respectively, according to the XRD data.[4]

7. Photothermal deflection spectroscopy

To directly verify the amount of FP8 in the doped FP5 single crystals, we used photothermal deflection spectroscopy (PDS), which typically a few orders of magnitude more sensitive to small optical densities of the sample than commonly used absorption UV–Vis spectroscopy.[8-9]The PDS signal was recorded with the use of a HeNe probe laser beam (633nm) and a two-section photodetector connected to a lock-in amplifier (SR830, Stanford Research). As a pump, monochromatized radiation of from a laser-driven broadband light source (EQ-99X, Energetiq) focused by a 0.94-NA parabolic mirror system was used. The pump beam was modulated by a mechanical chopper at a frequency of 24 Hz on which the lock-in amplifier was locked. The measurements were performed on free-standing crystals placed in a fused silica cuvette filled with perfluorohexane.

Figure S12 shows PDS spectra of FP5 single crystals. PDS spectra consist of the FP5 absorption edge and weak absorption features in the optical gap of the material. To calculate the amount of FP8 in the crystal, the spectra were fitted with the sum of Voigt (absorption edge of FP5) and Gauss (FP8) functions. The FP8 absorption band was fitted by a narrow band centered at 463±2 nm with a FWHM of 15 nm (Figure S12). Assuming that absorption of FP8 depends linearly on its concentration, the FP8 integrated absorption was used for calibration of FP8 concentrations (Figure S12, inset) in the samples with the prescribed FP8 concentrations.

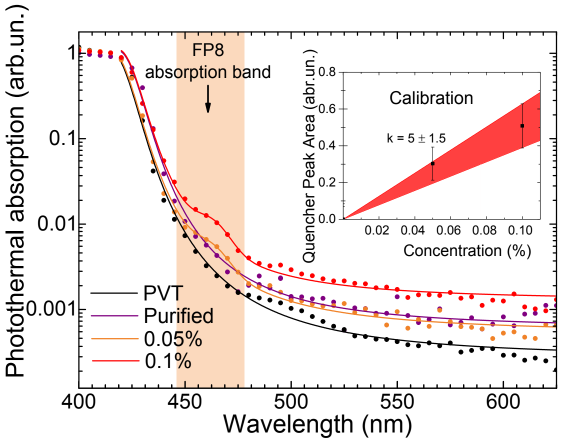

Figure S12. PDS spectra of FP5 single crystals. Dots show experimental data, lines are fits to the sum of Voigt (absorption edge of FP5) and Gauss (FP8) functions. The arrow indicates the position of the FP8 absorption band. Inset shows integrated FP8 absorption *vs.* prescribed FP8 concentrations; a direct proportionality fit was used for calibration to determine unknown FP8 concentrations; the uncertainty values were calculated from the PDS spectra fit.

Figure S13 shows the result of evaluation of concentration in purified and PVT crystals obtained from their PDS spectra. Both concentrations are well below the experimental sensitivity of ~0.01% which is mainly determined by the presence of the broad absorption tail extending deep into the optical gap and intersecting with the FP8 absorption band at 463 nm.

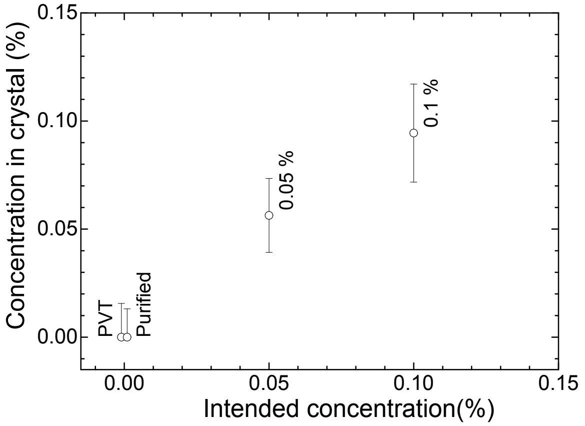

Figure S13. FP8 concentration in crystals calculated from the PDS data *vs.* the intended level of doping.

8. Transient red-shift of mean PL energy

A convenient way to characterize energy transport (as compared to spectrally-resolved PL transients, Figure 3) is to analyze the transient red shift of the mean PL energy; [10-11]the respective data are shown in Figure S14. For the PVT crystal, the excitons largely retain their initial energy around 2.59 eV. Nevertheless, a small red shift of 0.02 eV indicates residual contamination of the FP5 host with small amounts of FP8 (or possibly with other side products of the chemical synthesis). At the doping level of 0.025% and higher, the majority of excitons are transferred to the quencher (FP8) within the first nanosecond as evident from the long-time red-shifted PL, which is mostly attributed to the quencher PL spectral region (see Section 3.3 in the main text).

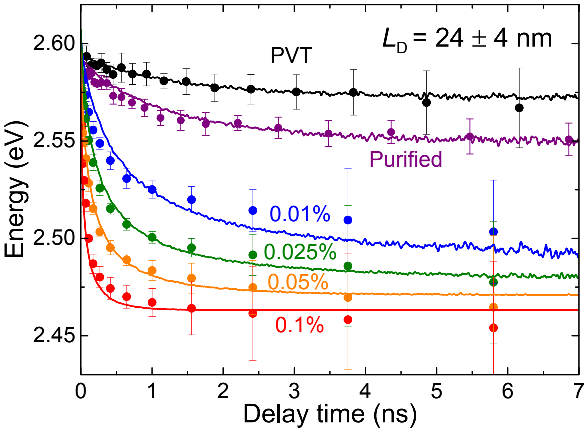

Figure S14. Experimental (circles) and MC simulated (lines) transient red-shifts of the mean PL energy for the representative doping levels: PVT (black), purified (purple), 0.01% (blue), 0.025% (olive), 0.05% (orange) and 0.1% (red) crystals. For the PVT (black) and purified crystal (purple) the quencher concentrations were retrieved by MC simulations as $8.5 \cdot 10^{-4}$% and 0.002%, respectively.

To retrieve the unknown quencher concentrations in the PVT and purified crystals (see discussion in the main text, Section 3.3), we simulated their transient red-shifts with concentrations as fit parameters (Figure S14, black and purple, respectively). The best agreement with the experimental data was achieved for 0.00085 % (PVT crystal) and 0.002% (purified crystal) concentrations of FP8. Note that these values should be taken with caution as they rely on the model used.

9. Thermal analysis

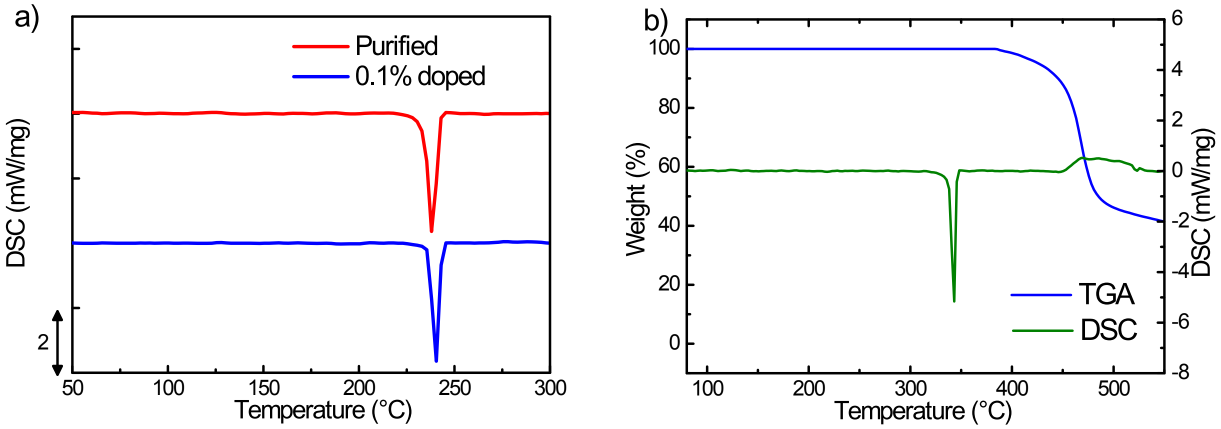

Figure S15. a) Differential scanning calorimetry data for purified and 0.1% doped FP5 single crystals. b) Thermal gravimetry (TGA) and differential scanning calorimetry (DSC) data for FP8.

10. Molecular dynamics simulations of FP8 in FP5 single crystal structure

Figure S16 illustrates how one FP8 molecule substitutes two (head-to-tail) host molecules in the FP5 single crystal structure. The pristine host (FP5) crystal molecular packing was taken from the x-ray diffraction data, [4] and the atoms rearrangements were simulated using molecular dynamics (MD) by "Avogadro: an open-source molecular builder and visualization tool."[12] The substitution results mainly in small torsional/bending deformations and adjustments of FP8, whereas the adjacent the FP5 conjugated cores maintain their initial positions (Figure S16).

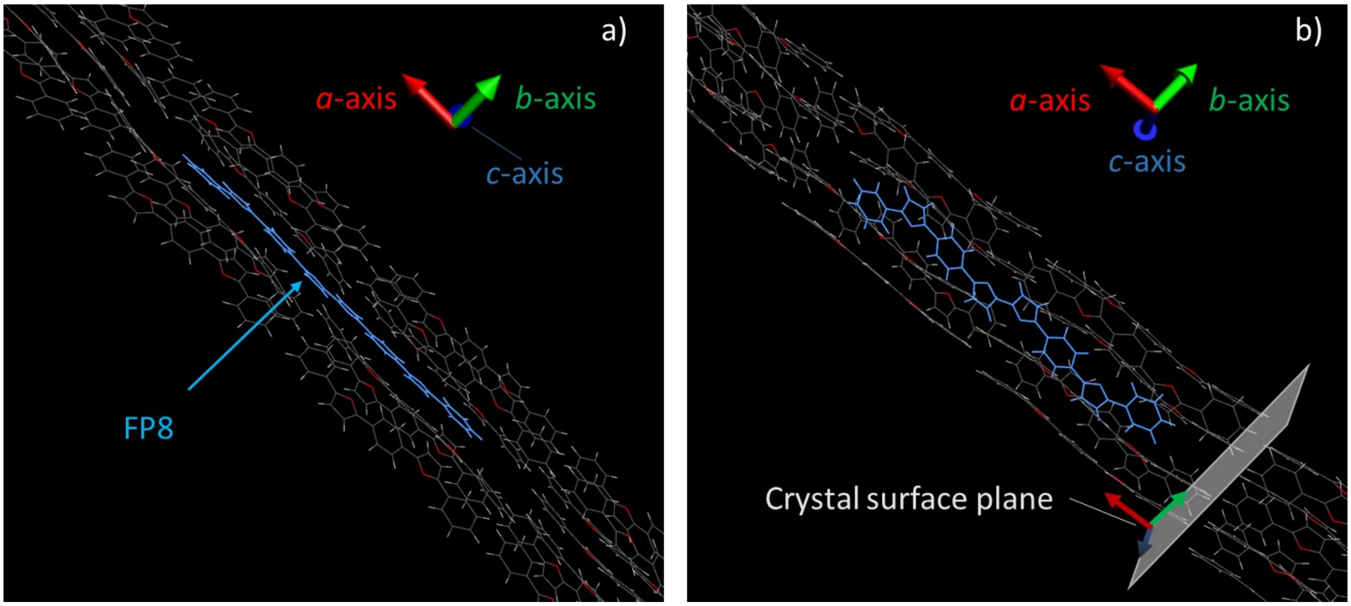

Figure S16. Model of an FP5 crystalline aggregate simulated for 28 molecules (7 for each layer), where the two central (head-to-tail) host molecules are substituted by a quencher (FP8). Red, green and blue arrows are the crystallographic *a*-, *b*- and *c*- axes, respectively, of the FP5 single crystal.[4] For better visibility, the orientation in panel (b) is turned by 45° around the crystallographic *a*-axis with respect to panel (a). Gray plane in (b) shows the orientation of the FP5 single crystal surface plane (100).

11. Polarization-resolved PL data

The results of the MD simulations were verified by polarization-sensitive time-resolved measurements in the following way. According to Ref. [4], the FP5 (host) and FP8 (quencher) transition dipole moments are directed from the meta position carbon atom of an outer phenylene to the opposite one (Figure S17a). The projection of these dipole moments onto the 100 plane of FP5 single crystal structure (this plane coincides with the surfaces of the crystal plates) to which the excitation beam is orthogonal and from which PL is collected, are shown in Figure S17b by yellow arrows. The projections of the FP5 transition dipole moment to the crystallographic *b*- and *c*- axes are almost equal (their ratio is ~0.93) while the projection of the FP8 transition dipole moment onto the crystallographic *c*-axis is approximately three times longer than its projection to *b*-axis (~2.9). This brings us to the following conclusion: PL originated from the FP5 (host) should be weakly polarized with the polarization ratio (similar to the corresponding parameter introduced in Ref.[13]) of $\rho_h = (0.93)^2 \approx 0.86$, while FP8 (quenchers) PL should be polarized along the crystallographic *c*-axis with $\rho_q = (0.35)^2 \approx 0.12$.

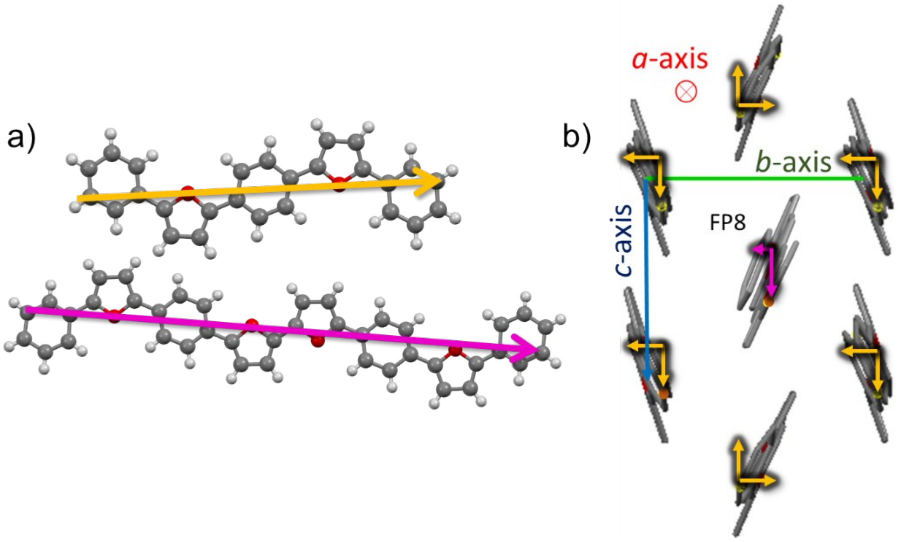

Figure S17. Transition dipole moments of FP5 and FP8 (yellow and pink arrows, respectively) [4] (a) and the view of the FP8-doped FP5 single crystal structure (Figure S16) along a-axis (b). The yellow and pink arrows in (b) show the projections of the FP5 and FP8 transition dipole moments on the b and c axes, respectively. The FP8 molecule in the center is surrounded by 14 FP5 molecules in the herringbone arrangement; for the ease of presentation only 6 of them are shown.

The results of polarization- and time-resolved PL measurements on the PVT and 0.1% doped crystals are shown in Figure S18; the figure orientation is identical to Figure S17b. First, we established that PL polarization for the PVT crystal does not depend on the polarization of the excitation radiation in agreement with the herringbone packing of FP5 molecules in the crystal structure.[4] Therefore, for practical reasons (ease of alignment) the excitation beam polarization was set parallel to one of the crystal edges (at 30° in Figure S18). To improve the contrast of PL anisotropic properties of the host crystal and the quenchers in the host crystal, we followed the logics of Figure 2 and discussion around it. Namely, PL of the PVT and 0.1% doped crystals were obtained in the time windows of 0–1 ns and 1–5 ns, respectively.

The short time (0–1 ns) PL decay is due to (yet) non-quenched host PL of the PVT crystal, and the long time (1–5 ns) window corresponds to the quencher PL in the 0.1% doped crystal (Figure S14, red).

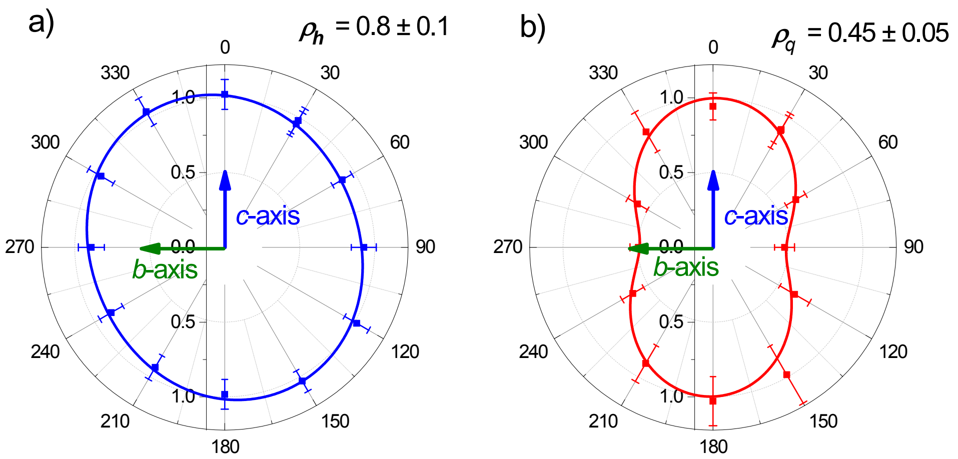

Figure S18. Polarization-resolved PL for the PVT crystal in the 0–1 ns (a) and 0.1% doped crystal in the 1–5 ns time window (b). The crystallographic axes *b*- and *c*- (olive and blue arrows, respectively) correspond to those in Figure S17b. The maximum PL intensity is normalized to unity. The solid lines are fits by the function $A \cdot cos^2(\theta - \theta_0) + B$, where θ is the angle between polarizations of PL and the crystallographic *c*-axis, while A, B and θ_0 are the fitting parameters. The polarization ratio ρ for host and quencher PL bands were calculated as $\rho = B/(A + B)$.[13] The excitation wavelength was set at 375 nm.

Host PL (Figure S18a) is nearly non-polarized ($\rho_h = 0.8 \pm 0.1$), which is in line with the results of MD simulations (Figure S17b). Quenchers PL in the doped crystals (Figure S18b) shows a notable anisotropy with the preferential direction along the *c*-axis and the polarization ratio of $\rho_q = 0.45 \pm 0.05$. Again, this result is consistent with the MD simulations albeit the experimental anisotropy is somewhat higher than theoretically-predicted, which might be due to polarization scrambling in the microscope objective. All in all, the polarization-resolved measurements confirm the model in Figure S16 thereby giving credit to the supposition of smooth embedding of the quencher into the host lattice.

12. Calculations of the orientation factor in Förster radius

With MD simulations of the molecular structure in the doped crystals (Section 10) at hand, we are in a position to evaluate the orientation factor γ^2 in Eq.S1. For this, we calculated the dipole-dipole interaction energy between the quencher and two nearest shells of host molecules (14 and 24 molecules are in the first and second shells, respectively):[7]

$$E_{dip-dip} \sim \gamma \cdot r^{-3} = [\cos\beta_{DA} - 3 \cdot \cos\beta_A \cdot \cos\beta_D] \cdot r^{-3}, \qquad \text{(S2)}$$

where β_{DA} is the angle between the direction of the transition dipole moments of the donor and acceptor molecules located at the distance r, β_A and β_D are the angles between the line connecting the centers of the acceptor and donor molecules, respectively, and their transition dipole moments. Figure S19 shows the distribution of these interaction energies from which $<\gamma>^2$ was estimated as ~1.5.

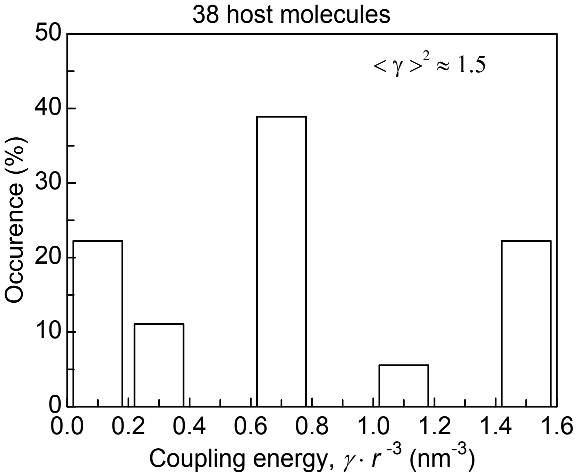

Figure S19. Distribution of the dipole-dipole interaction energies for a quencher (FP8) surrounded by 38 host (FP5) molecules.

13. Photoluminescence maps

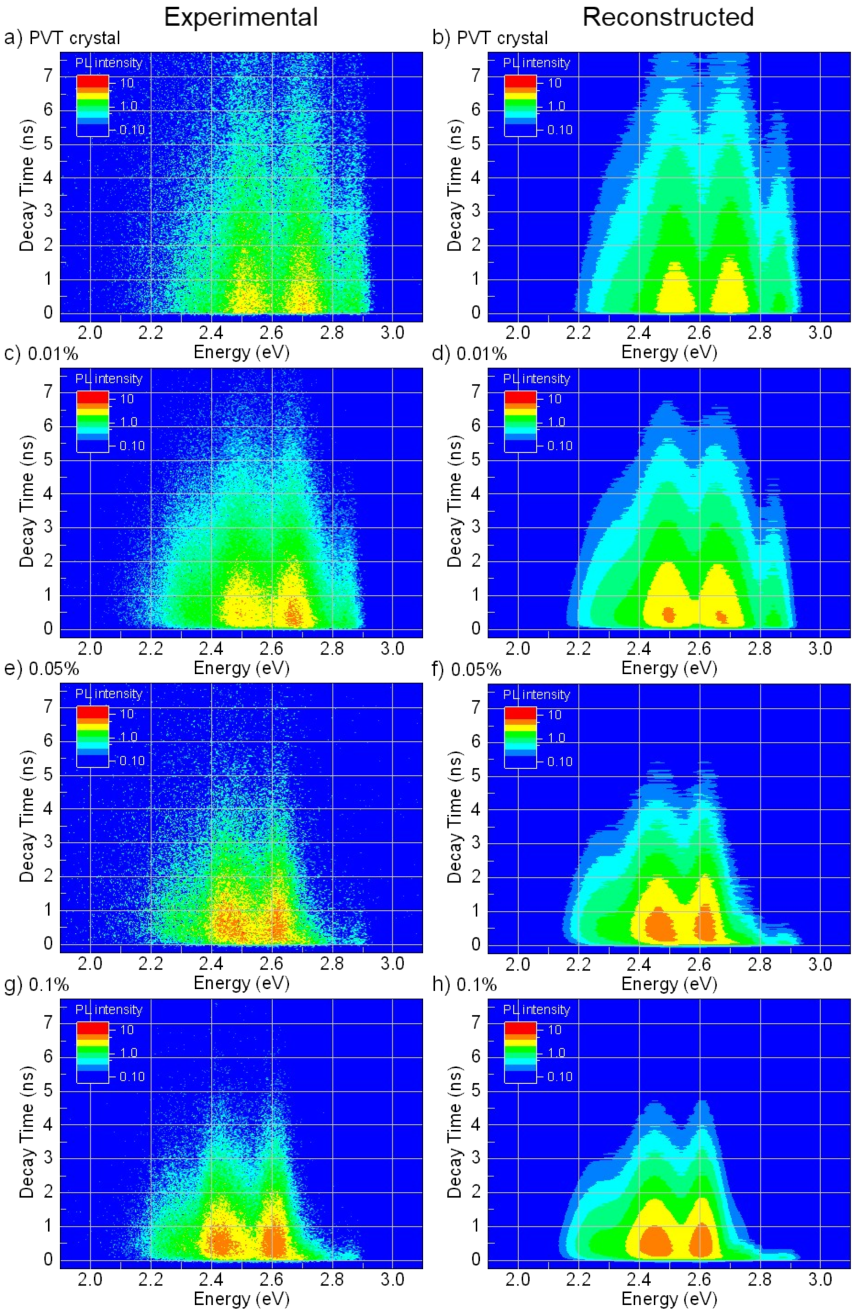

Figure S20. Experimental (left column) and reconstructed (right column) PL maps of variously doped FP5 single crystals (the quencher concentration is shown in the panels). The reconstructed PL maps are obtained as the weighted sum of the reference host and quencher spectra (shown in Figure 2) for each time step of 1 ps. Note the logarithmic scale of the color-coding. The excitation wavelength was set at 375 nm. The resulted shares of both spectra are depicted in Figure 3.

14. Quencher-quencher mean distance

Assuming that the quencher molecules are homogeneously distributed in the doped crystal, the mean distance *d,* between the nearest quenchers in the crystals with the molar doping level n_d was calculated as:

$$d = \sqrt[3]{\frac{M}{\rho\, N_A\, n_d}} = \sqrt[3]{\frac{1}{n_d}} \cdot 0.78\ [nm] \quad , \tag{S3}$$

where $M = 370$ g·mol^{-1} is the host (FP5) molar mass, $\rho = 1.316$ g·cm^{-3} is the host crystal density.[4]

15. MC simulations parameters

Table S1 lists the parameters used in MC simulations; most of them are directly extracted from the prior experimental data (marked as "Input" in Table S1). The only free parameter (marked as "free" in Table S1), is the hopping time τ_{hop} which was obtained from the best approximation of the experimental data for the full set of doped crystals.

To evaluate the stability of MC results, we tested the goodness of the fit by the least squared deviation as a criterion:

$$\chi^2 \equiv C \cdot \sum_i \sum_m \left(E_{data}(t) - E_{MC}(t)\right)^2 \tag{S4}$$

where $E_{data}(t)$ is the experimental value of the mean PL energy at the time moment t, $E_{MC}(t)$ is the corresponded MC value, *m* is number of data points, *i* is the crystal index (*i* = 1, 2, 3, 4 stand for the 0.01%, 0.025%, 0.05%, 0.1% doping levels, respectively), and C is the normalization coefficient (~1/eV^2) chosen in such a way to normalize the minimal χ^2 value to unity. Figure S21 shows that the MC simulations are stable with respect to variations in the exciton diffusion length (the output parameter of the MC simulations) and the host PL QY. We fixed the ratio of QYs of the host and quencher to the experimental value of 0.7 because the measurements of the relative QYs are much more accurate than their absolute values. As evident from Figure S21, the χ^2 value is very weakly dependent on PL QYs but is sharply dependent on the exciton diffusion length thereby demonstrating good convergence of the MC simulations.

Table S1. Global parameters (input, free, and output) of the Monte-Carlo simulation for the four crystals (0.01%, 0.025%, 0.05%, 0.1% doping levels). The uncertainty margins for the input parameters are given according to the accuracy of the measured data. The error margins for the free parameters were obtained according to the χ^2 minimization procedure.

Parameter (units)	Value at 293 K	Type (Source)
Mean host photon energy, $E_0 + \Delta E$ (eV)	2.6 ± 0.02	Input (Figure 2)
Mean quencher photon energy, E_0 (eV)	2.46 ± 0.02	Input (Figure 2)
Donor-acceptor energy gap, ΔE (eV)	0.14 ± 0.02	Input (Figure 2)
Exciton lifetime in host matrix, τ (ns)	2.9 ± 0.2	Input (Figure 4a)
Excitation lifetime of quenchers, τ_q (ns)	1.4 ± 0.1	Input (Figure 4a)
PL QY of host matrix, QY_h (%)	50 ± 5	Input (Figure 6)
PL QY of quenchers, QY_q (%)	70 ± 5	Input (Figure 6)
Host radiative lifetime, τ_r (ns)	5.8 ± 0.2	Obtained from τ and QY_h
Quencher radiative lifetime, τ_{qr} (ns)	1.5 ± 0.2	Obtained from τ_q and QY_q
Host non-radiative lifetime, τ_n (ns)	5.6 ± 0.5	Obtained from τ and QY_h
Quencher non-radiative lifetime, τ_{qn} (ns)	4.5 ± 0.4	Obtained from τ_q and QY_q
Förster radius, R_0 (nm)	4.9 ± 0.5	Input (SI, Section 4)
Hopping time, τ_{hop} (ps)	1.5± 0.5	Free
Diffusion length, L_D (nm)	24 ± 4	Output

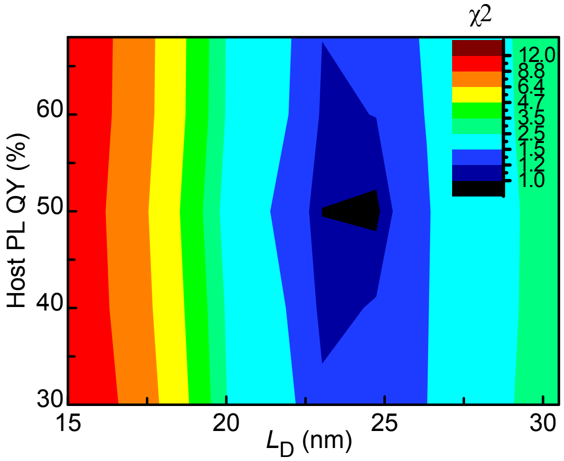

Figure S21. χ^2 map of the least squared deviations between the MC calculations and experimental data for the FP5 single crystals as a function of the host PL QY and exciton diffusion length, L_D. The QY_h/QY_q=0.7 ratio was fixed. The global minimum value of χ^2 and its width determine the values and uncertainties, respectively, of the global parameter L_D = 24 ± 4 nm

16. Distributions of the exciton displacements for the volume PL quenching method

Figure S22 shows the exciton displacement (i.e. the distance between the initial and final positions) distributions for all excitons in the host matrix. Initially, the excitons (one exciton per $1.3 \cdot 10^5$ FP5 molecules; for details, see Section 19 are randomly distributed over the crystal matrix in such a way that an exciton is never placed on the cell which is already occupied by another exciton (or a quencher). The final exciton position is the one where the exciton ceases to exist (i.e. it either decays radiatively or non-radiatively, or is transferred to the quencher). The exciton diffusion lengths are directly calculated from the distributions as their mean values.

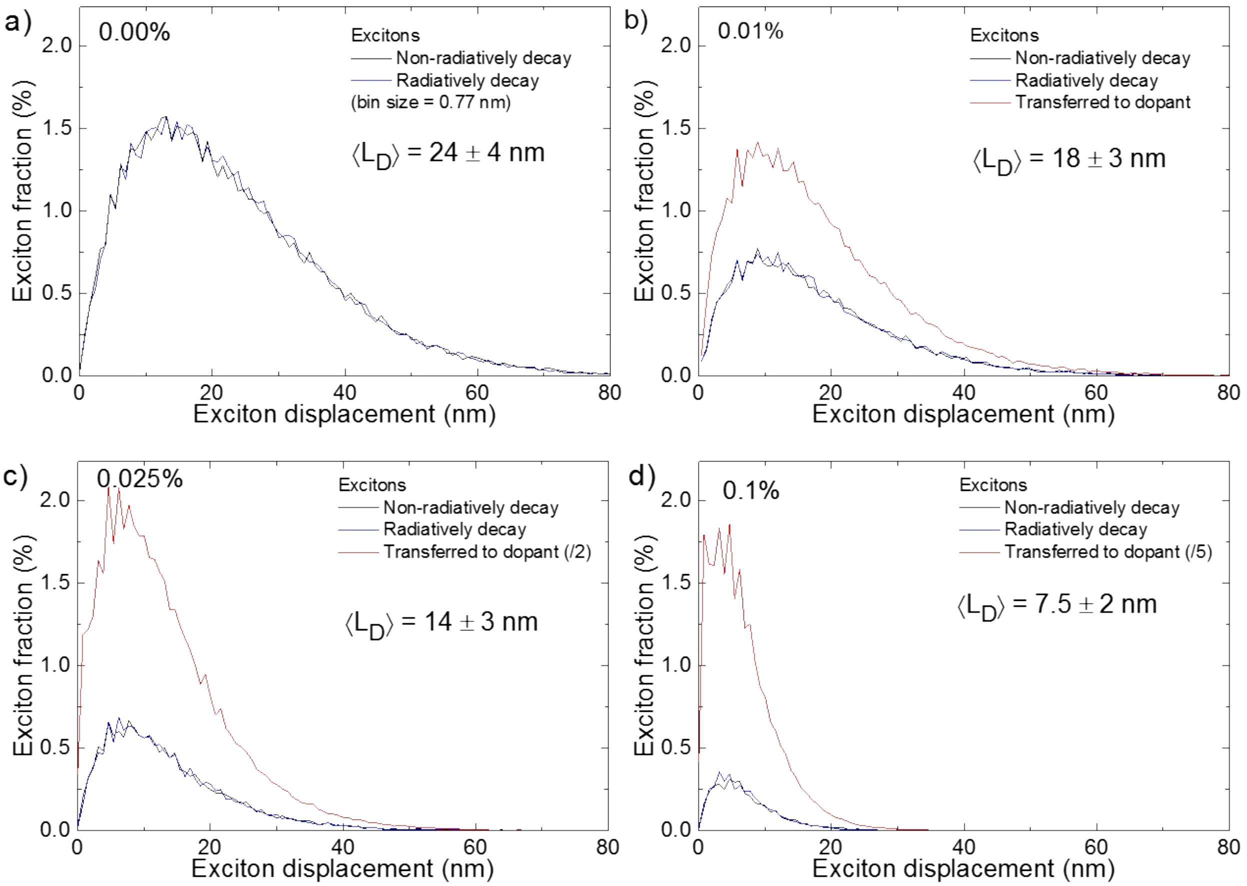

Figure S22. Distributions of exciton displacements in variously doped crystals in the quenching volume method. The quencher concentrations and mean exciton diffusion lengths L_D are shown in the respected panels. Red curves: excitons transferred to the quenchers via FRET (the final FRET step is not included); blue curves: radiatively decaying excitons; black curves: non-radiatively decaying excitons.

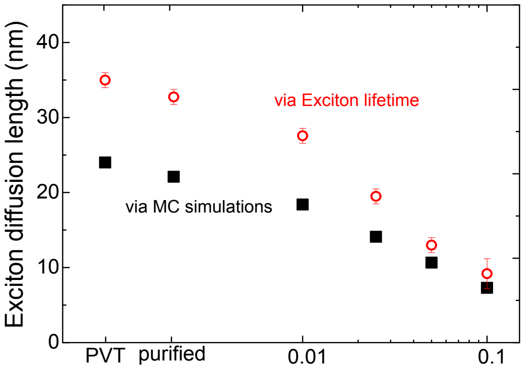

Figure S23. Exciton diffusion length as derived from MC simulations (black) and from host exciton lifetime (blue-flank decay) for variously doped FP5 single crystals.

17. Singlet exciton diffusion length in various organic single crystals

Table S2. Singlet exciton diffusion length in various organic single crystals measured via PL methods

Crystalline structure	L_D, nm	Reference	Technique
Naphthalene	50[a)]	Gallus *et al.*[14]	Surface PL quenching
Anthracene	60[a)]	Mulder[15]	Surface PL quenching
Phenanthrene	8	Gillus *et al.*[16]	Surface PL quenching
Tetracene	12	Vaubel *et al.*[17]	Exciton-exciton annihilation and surface PL quenching
PTCDA	25[b)]	Lunt *et al.*[18]	Volume PL quenching with QY measurements
TMS-PTTP-TMS	2.5	Parashchuk *et al.*[5]	Time-resolved volume PL quenching

[a)] There might be a contribution from triplet excitons due to the ultrafast singlet-to-triplet conversion and subsequent delayed triplet-to-singlet conversion. [19-21]

[b)] The data were measured for polycrystalline films and extrapolated for single crystals.

18. Excitation intensity

For long exciton diffusion lengths, exciton-exciton annihilation[22] presents a serious challenge as the excitation intensity should be attenuated to the values where the probability of two excitons to meet becomes negligibly low. Therefore, we carefully investigated PL decays in the PVT crystal (where the exciton diffusion is the longest) in a broad range of excitation fluxes of 0.5–50 μJ/cm^2 (i.e. peak power was ranged in 0.625 – 62.5 W). To achieve such fluxes, we placed the microscope objective focus (~4 μm in diameter; ~12.5 μm^2 in area) right onto the crystal surface. The excitation spot size was measured by imaging the laser beam focused on a silicon wafer placed in the objective focus.

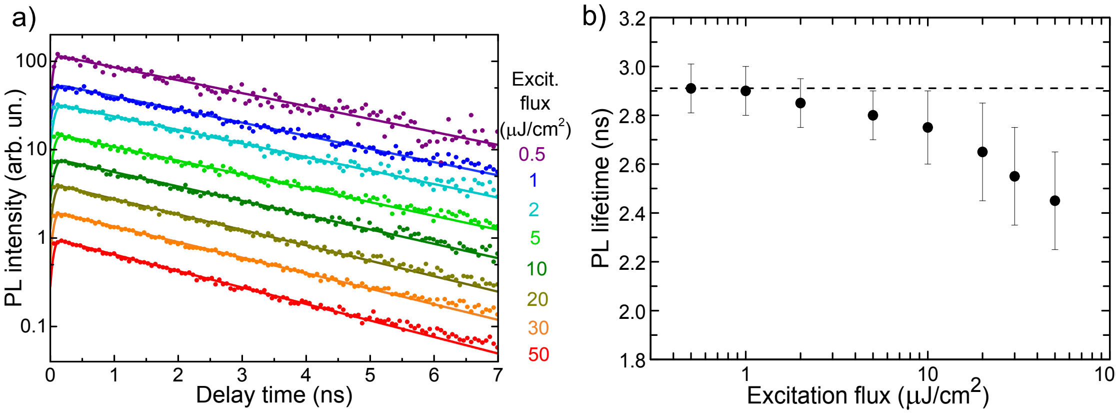

Figure S24. Experimental (dots) PL transients (a) and PL lifetimes (b) under various excitation flux in the PVT crystal. The solid lines in panel (a) are the monoexponential fit of the PL transients. PL lifetimes shown in panel (b) are extracted from the fits. The dash line represents the PL lifetime of the host (2.9 ns). The excitation wavelength was set at 375 nm.

The respective PL transients with exponential fits (Figure S24a) show clear evidence of exciton-exciton annihilation (in a separate experiment we established that this is not caused by sample photodegradation). The decay times obtained from the monoexponential fits are summarized in Figure S24b as a function of excitation intensity. With the decrease of excitation flux, PL lifetime increases indicating the reduction of exciton annihilation. At the excitation flux below ~5 μJ/cm^2 the decay time converges to ~2.9 ns, which is the host exciton lifetime, where the exciton annihilation becomes negligible. Accordingly, all other experiments were performed at the excitation intensity of 1 μJ/cm^2.

19. Calculations of the mean distance between the excitons in the annihilation experiments

The density of excitations for the excitation flux of 1 μJ/cm^2, is estimated as ~$1.5 \cdot 10^{16}$ cm^{-3} (the crystal thickness of ~1 μm and the sample absorbance of OD~0.5 at the excitation wavelength 375 nm). Thus, at the excitation flux of 1 μJ/cm^2 one exciton exists in the ~40x40x40 nm^3 volume, i.e. the mean distance between the excitons is $d_{\text{e-e}}$=40 nm.

For MC simulations on annihilation, we need to know the number of excitons per one unit cell. The density of molecules in the FP5 single crystal[4] is ~$2\cdot10^{21}$ cm^{-3} which results in the averaged crystal unit cell size of ~0.77 nm, or one exciton per $1.3\cdot10^5$ FP5 molecules for the excitation flux of 1 μJ/cm^2.

20. Monte-Carlo simulation for the exciton-exciton annihilation technique

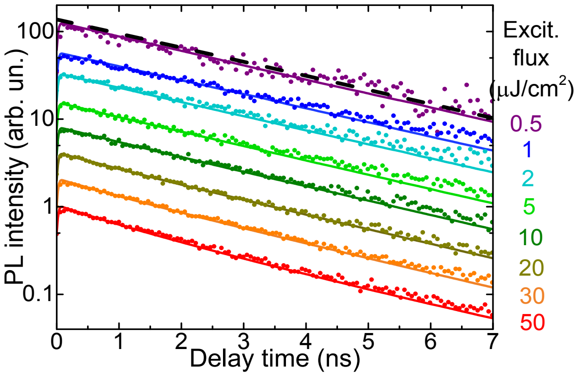

Figure S25. Experimental (dots) and Monte-Carlo simulated (lines) PL transients under various excitation fluxes in the PVT crystal. In the MC simulations, the annihilation radius, R_a, was set as the average unit cell size (0.77 nm).

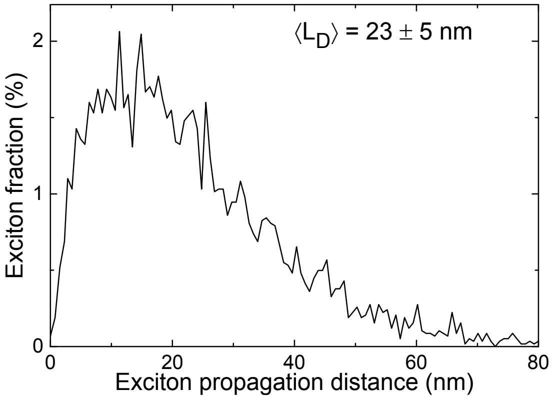

Figure S26. MC simulated distribution of exciton displacements in the PVT FP5 single crystal for the lowest excitation flux (i.e. in the absence of exciton-exciton annihilation). The bin size in the horizontal axis is 0.77 nm.

21. Energy transfer efficiency

Figure S27 shows quantum efficiency of energy transfer defined as a ratio of the number of excitons transferred to the quenchers to the number of initial excitons in the crystals. With the increase of quencher concentration, the energy transfer efficiency reaches ~90% in the 0.1% doped crystal.

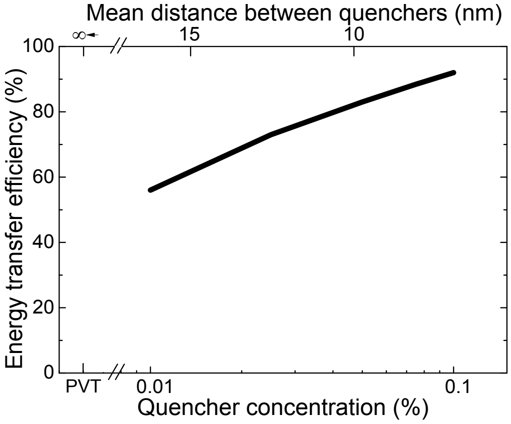

Figure S27. Monte-Carlo simulated energy transfer efficiency from the host excitons to the quenchers. The upper axis shows a mean distance between quenchers in the host crystals (for details see SI, Section 14)

22. Steady-state PL spectra in doped crystals

Figure S28 plots steady-state PL spectra of variously doped FP5 single crystals. Similarly to the PL spectra recorded with the use of the streak-camera (Figure 2), the PL spectra shift to the red with the increase of doping level (FP8 concentration) due to FRET from the FP5 matrix to FP8. Note that the red shift in Figure S28 with doping is partially related to the PL reabsorption effect Ref.[5]

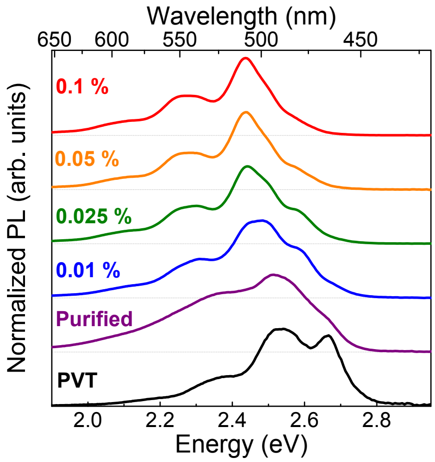

Figure S28. Steady-state PL spectra of variously doped FP5 single crystals recorded with the use of the integrating sphere. The excitation wavelength was 405 nm.

23. Charge transport in doped single crystals

Fabrication and characterization

Organic field-effect transistors (OFETs) were fabricated using the top-contact top-gate configuration.[23] The carefully selected (for not having any visible defects and cracks) single crystals were attached to the glass substrates by cyanoacrylate glue. Source and drain contacts were painted on the surface of the crystals by colloidal graphite paste (PELCO, TED PELLA, INC). As a top dielectric layer, a 1.5-µm-thick film of parylene N) was deposited from [2,2]paracyclophane (Sigma Aldrich). The gate electrode was painted using graphite paste. OFET current-voltage characteristics were recorded using a source-meter instrument (Agilent B2902A) at ambient conditions. The voltage sweep rate was 1.2 Vs^{-1}. The field-effect mobility was calculated in the saturation regime according to the Shockley model:[24]

$$I_{sd}^{1/2} = \left(\frac{W}{2L}\mu\, C\right)^{1/2}(V_g - V_{th})\;, \qquad \text{(S5)}$$

where I_{sd} is the source-drain current; V_g and V_{th} are the gate and threshold voltages, respectively; C is the capacitance per unit area of the insulating layer (1.6 nF/cm^2); W and L are the channel width and length, correspondingly; μ is the carrier mobility.

OFET data

Images of the OFET device based on a 0.1% doped FP5 single crystal are shown in Figure 29. The images demonstrate no visible defects, which might severely affect the charge transport measurements. All OFET devices demonstrated *p*-type characteristics. Figure S30a demonstrates transfer characteristics of purified (a) and 0.1% doped (b) single-crystal OFETs; the latter shows the lower charge mobility and the higher threshold voltage. The full OFET data are presented in Table S3.

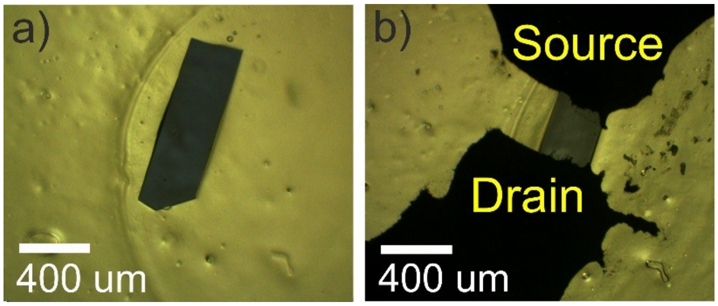

Figure S29. Optical images of a 0.1% doped FP5 single crystal used for OFET fabrication: before (a) and after (b) deposition of graphite contacts.

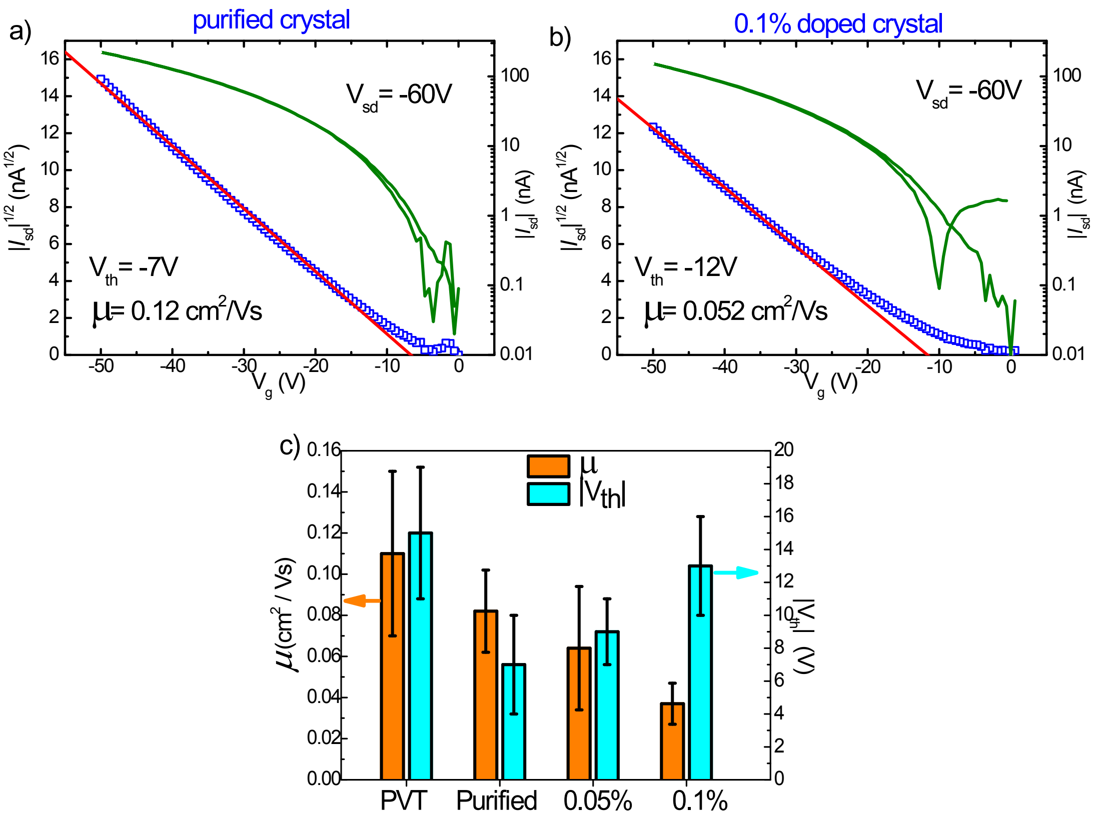

Figure S30. Single-crystal OFET devices. Transfer characteristics for purified (a) and 0.1% doped (b) FP5; (c) average mobility (orange bars) and modulus of threshold voltage (cyan bars) for various crystals. The data for the PVT crystal are from Ref.[25]

Table S3. Parameters of single-crystal OFETs.

Crystal type	Sample	W (mm)	L (mm)	W/L	μ (cm^2/Vs)	V_{th} (V)
Purified	1	2.13	0.82	2.60	0.067	-5
	2	1.69	0.69	2.45	0.073	-12
	3	1.30	0.60	2.16	0.103	-5
	4	0.78	0.60	1.30	0.066	-10
	5	1.48	0.70	2.11	0.050	-9
	6	0.61	0.53	1.15	0.122	-6
	7	1.11	0.53	2.10	0.106	-7
	8	0.61	0.46	1.32	0.090	-3
	9	0.65	0.51	1.27	0.062	-3
				average:	0.082±0.02	-7±3
0.05	10	0.52	0.37	1.40	0.030	-6
	11	0.35	0.47	0.74	0.037	-11
	12	0.62	0.37	1.67	0.020	-10
	13	1.05	1.09	0.96	0.086	-11
	14	0.73	0.51	1.43	0.096	-5
	15	0.40	0.44	0.91	0.077	-8
	16	0.82	0.55	1.49	0.087	-8
	17	0.57	0.53	1.07	0.082	-10
				average:	0.065±0.03	-9±2
0.1	18	0.31	0.34	0.91	0.026	-17
	19	0.61	0.45	1.35	0.027	-9
	20	0.86	0.43	2.00	0.052	-12
	21	1.22	0.50	2.44	0.035	-13
	22	0.50	0.72	0.69	0.048	-13
				average:	0.038±0.01	-13±3

24. Energies of frontier molecular orbitals

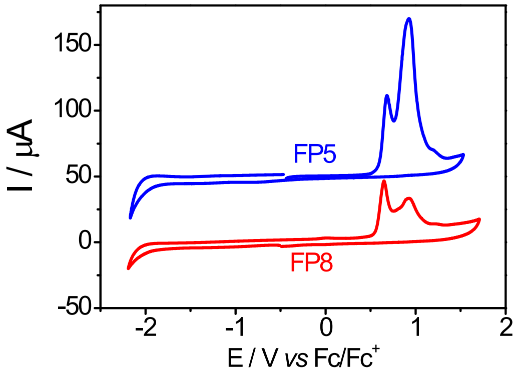

Figure S31. Cyclic voltammogramms of FP5 (blue) and FP8 (red) measured for thin films deposited on the surface of working electrode immersed in CH_3CN solution.

Table S4. Summary of the energies of the frontier molecular orbitals of FP5 and FP8 with the related energy gaps.

	E_{HOMO}, eV	E_{LUMO}, eV	E_g, eV
FP5	-5.39[a]/-5.08[b]	-2.30[a]/-1.82[b]	3.09[a]/3.26[b]
FP8	-5.35[a]/-4.86[b]	-2.55[a]/-2.00[b]	2.83[a]/2.86[b]
Energy gap between FP8 and FP5	0.04[a]/0.22[b]	0.25[a]/0.18[b]	-

[a] Experimental data: HOMO (estimated from CVA) and LUMO (calculated *via* $E_{\mathrm{LUMO}} = E_{\mathrm{HOMO}} + E_g$, where E_g is the optical gap estimated from the intersection point of absorption and PL spectra); [b] Quantum chemical calculations were performed using ORCA 4.0.1 package. The ground state geometries of neutral, anionic and cationic forms of investigated compounds were fully optimized using hybrid B3LYP functional coupled with 6-311++G** basis set. The presence of imaginary frequencies was checked in harmonic approximation for all investigated geometries, and minima of the potential energy surface were found to be «genuine».

25. Organic light-emitting transistors

Fabrication and characterization

Si/SiO_2 substrates with thermally-grown 200-nm thick oxide layer were sonicated in isopropanol for 15 minutes at 70°C, rinsed by distillated water, dried in argon flow and treated by ultraviolet radiation for 15 minutes. All following stages of device preparation and characterization were conducted in inert atmosphere in argon-filled gloveboxes. For PVT single-crystal and vacuum-deposited OLETs, a 30-nm-thick poly(methylmethacrylate) PMMA layer was spin-coated on the substrates at 3000 rpm from 10 mg/mL solution in toluene, and then the substrates were annealed at 70°C for 20 hours and at 110°C for 3 hours in vacuum oven.

Three different types of OLET active layers were prepared: ultrathin crystals grown from solution of raw and purified FP5 directly on the substrate, vacuum deposited thin films from purified FP5, and PVT-grown FP5 single crystals. Ultrathin single crystals were grown on Si/SiO_2 substrates from 0.21 mg/mL solution in o-dichlorobenzene: first, the solution was spincoated on the substrates at 600 rpm for 30 s, then the substrates were placed in Petri dishes for 19 hours to let the crystals grow in saturated solvent vapor.[26] A thin-film polycrystalline active layer was thermally evaporated in a vacuum chamber at pressure of $3.1 \cdot 10^{-6}$ mbar with 1-6 Å/s evaporation rate, the thickness was 15 nm according to a thickness monitor (TM400, Maxtek). PVT single crystals were laminated on Si/SiO_2 substrates covered by PMMA.

Ca and Au metal electrodes were thermally deposited on the active layer in vacuum at pressure lower than $2 \cdot 10^{-6}$ mbar. Shadow masks were used to form the source and drain electrodes (20 devices on a substrate) with different channel lengths (L) from 10 to 30 μm with a step of 5 μm and a channel width (W) of 1 mm. The evaporation rate of Ca was 0.3 – 0.4 Å/s, the evaporation rate of Au was 4 – 13 Å/s. The electrode thickness was 30.0 nm according to the thickness monitor). Asymmetric deposition of the Ca/Au electrodes was realized via the shadow effect. As a result, at one electrode, a part of the Ca underlayer was maintained in a direct contact with the active layer hence worked as the electron-injecting electrode. On the opposed electrode, the Au overlay film had a direct contact with the active layer and acted as the hole-injecting electrode.[27] As a gate electrode the n-doped Si substrate was used.

Output and transfer characteristics (dependences of source-drain current I_{SD} on source-drain voltage V_d and source-gate voltage V_g, respectively) of the OLET devices were measured using a probe station (PrintElTech) and Keithley Sourcemeter 2636A. The charge carrier mobility and the threshold voltage in the saturation regime were calculated by an approximation of the measured transfer characteristics to the Shockley equations. Light emission was captured by a CCD camera (Infinity 3, Luminera) equipped by a microscope objective (Mitutoyo M Plan Apo 10x/0.28) at an exposition of 60 s during the measurement of transfer characteristics. Thicknesses of OLET active layers were measured by using an atomic-force microscope (AFM Ntegra Spectra, NT-MDT).

OLET data

25.2.1 Solution-grown active layer

Figure S32a shows transfer characteristics of OLETs based on the crystals grown from solution on substrate by using raw and purified FP5; the images of the respective OLET devices are shown in panels (c) and (e), correspondingly. The channel of each device contains several single crystals. The device based on raw FP5 has L= 15 μm and W=124 μm (over all crystals in the channel), and the latter has L=25 μm and W=177 μm (over all crystals in the channel). The crystal thicknesses are in the range of 20–60 nm.

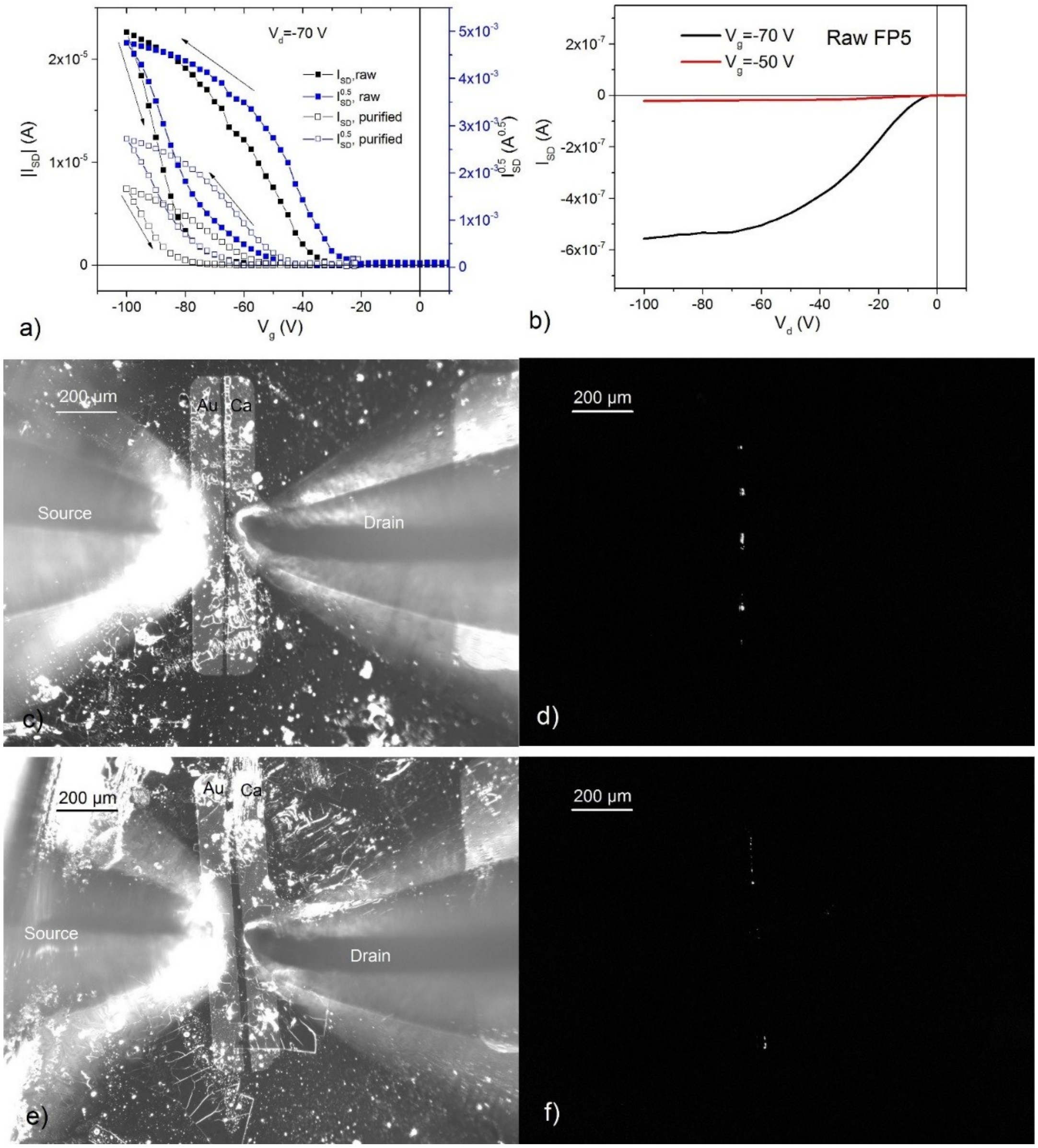

Figure S32. OLETs based on the active layer grown on a substrate from raw and purified FP5. Transfer (a) and output (b) characteristics. OLET images based on the raw and purified FP5 are shown in panels (c, d) and (e, f), respectively. Images in panels (c, e) are captured with the backlight; images in panels (d, f) were taken in the dark. In all OLET images here and below the hole-injecting electrode (Au) is on the left, and electron-injecting electrode (Ca) is on the right.

25.2.2 Vacuum-deposited active layer

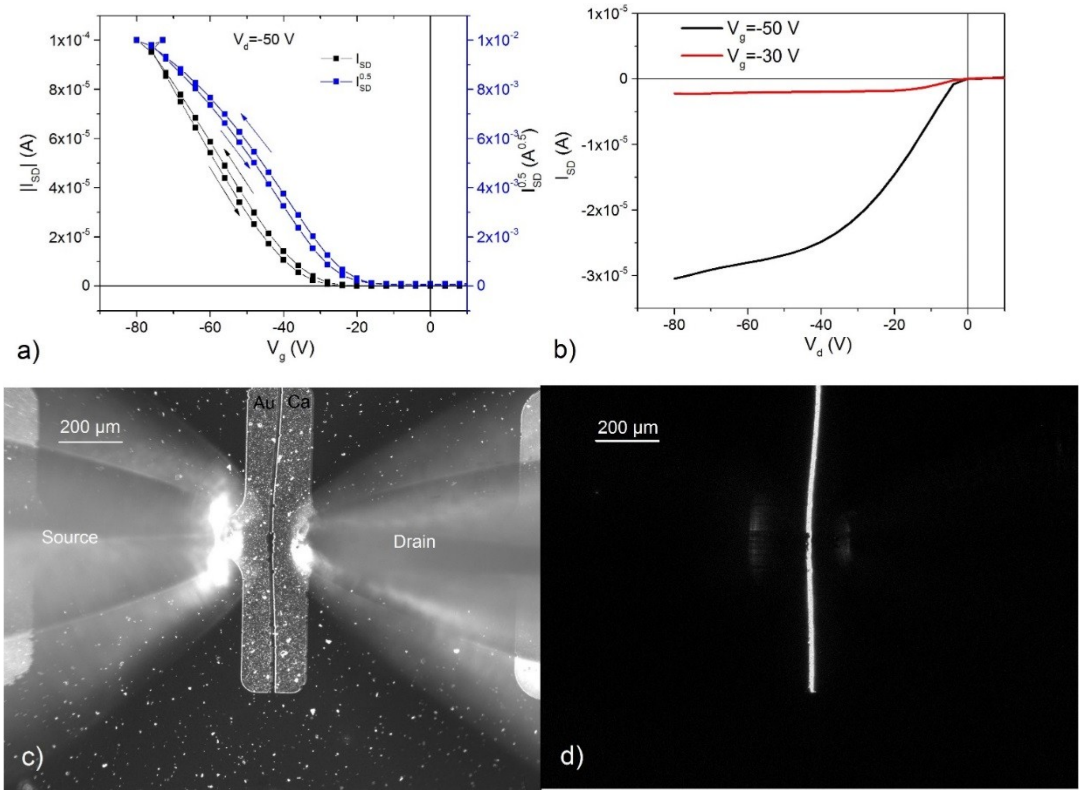

Figure S33. OLET based on a vacuum-deposited FP5 active layer. Transfer (a) and output (b) characteristics, OLET images with the backlight (c) and in the dark (d). *L*=10 µm and *W*=1000 µm, the film thickness is 19±6 nm.

25.2.3 PVT single crystal as active layer

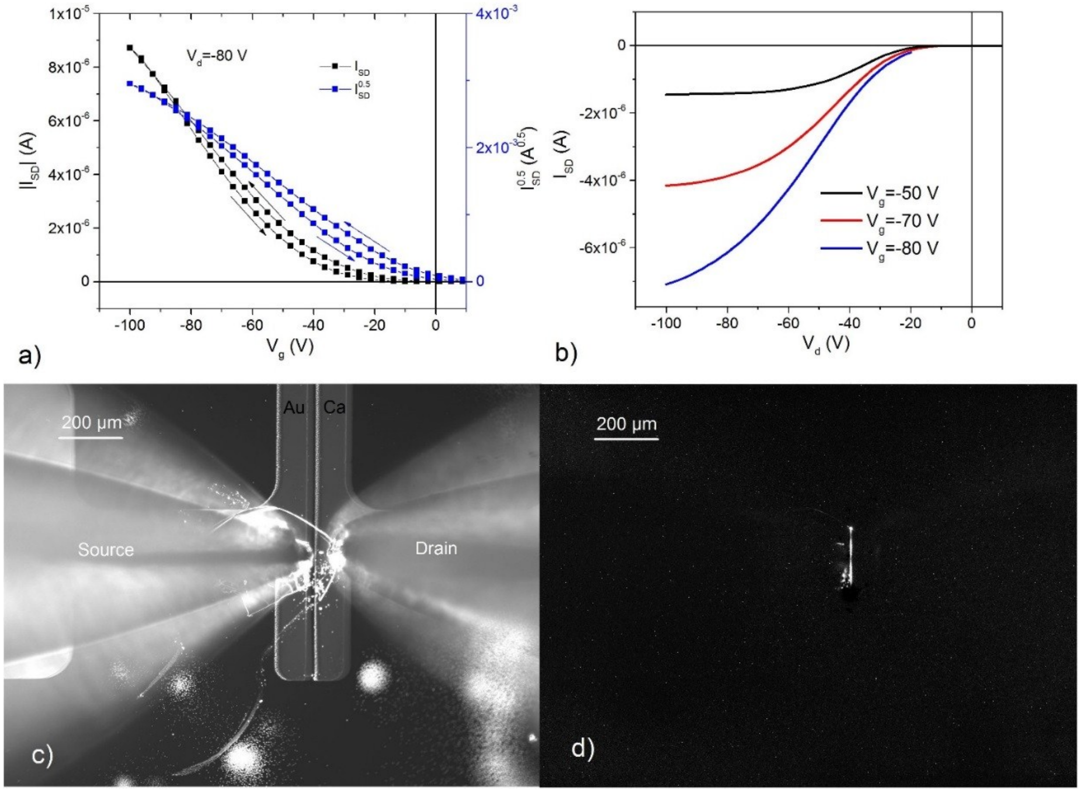

Figure S34. OLET based on a FP5 PVT single crystal. Transfer (a) and output (b) characteristics, OLET images with the backlight (c) and in the dark (d), *L*=25 µm, *W*=193 µm, the thickness of the single crystal is about 900 nm.

25.2.4 Discussion

The calculated hole mobilities and threshold voltages of all OLET devices prepared in this work are summarized in Table S4. All OLETs worked in the unipolar hole transport regime. Light emission was brighter for the active layers deposited from the vapor phase: the light intensities per channel width are higher by 17% for the vacuum-deposited film OLET and by 49% for the PVT-crystal based OLET with respect to the solution-grown-crystal OLET (Table S5). Moreover, the threshold voltages and hysteresis for them were lower than those of the solution-prepared OLET active layers. The higher performance for the active layers deposited from the vapor phase can be assigned to benefits of vapor deposition and the passivation effect of a PMMA layer between FP5 and SiO_2.[27] For the solution-processed active layers, we tried to passivate the SiO_2 dielectric by hexamethyldisilazane (HMDS); however, due to low wettability of the used organic solvent (DCB), we did not manage to grow crystals of enough lateral sizes on substrates coated with HMDS.

Table S5. OLET parameters. Charge carrier (hole) mobilities, μ, and threshold voltages, V_{th}, in the saturation regime for forward and backward scans of current-voltage characteristics measurements. Light emission intensities per channel width, I_W, were calculated from the OLET images in the dark (Figure S32 – S34) as a sum of intensities of all pixels divided by W.

OLET active layer	FP5	W (μm)	L (μm)	W/L	I_W (arb.units)	Scan direction	μ (cm^2/Vs)	V_{th} (V)
Solution-grown	Raw	124	15	8.27	1	forward	0.28±0.05	–28±4
						backward	0.034±0.007	–48±8
Solution-grown	Purified	177	25	7.08	0.58	forward	0.116±0.007	–44.7±0.7
						backward	0.059±0.021	–26±23
Vacuum-deposited	Purified	1000	10	100	1.17	forward	0.070±0.003	–24.8±1.1
						backward	0.068±0.004	–22.3±1.2
PVT	Purified	193	25	7.72	1.49	forward	0.0232±0.0007	–8.2±0.8
						backward	0.0284±0.0009	–16.9±0.9

26. References

(1) SAINT Bruker Analytical X-ray System: Wisconsin, USA-2006, 1997.

(2) Sheldrick, G. M. *Sadabs* Institute for Inorganic Chemistry, 1996.

(3) Sheldrick, G. M. A Short History of Shelx. *Acta Crystallogr. Sect. A: Found. Crystallogr.* **2008**, *64*, 112-122.

(4) Kazantsev, M. S.; Frantseva, E. S.; Kudriashova, L. G.; Konstantinov, V. G.; Mannanov, A. A.; Rybalova, T. V.; Karpova, E. V.; Shundrina, I. K.; Kamaev, G. N.; Pshenichnikov, M. S.; Mostovich, E. A.; Paraschuk, D. Y. Highly-Emissive Solution-Grown Furan/Phenylene Co-Oligomer Single Crystals. *RSC Adv.* **2016**, *6*, 92325-92329.

(5) Parashchuk, O. D.; Mannanov, A. A.; Konstantinov, V. G.; Dominskiy, D. I.; Surin, N. M.; Borshchev, O. V.; Ponomarenko, S. A.; Pshenichnikov, M. S.; Paraschuk, D. Y. Molecular Self-Doping Controls Luminescence of Pure Organic Single Crystals. *Adv. Funct. Mater.* **2018**, *28*, 1800116.

(6) Kazantsev, M. S.; Beloborodova, A. A.; Kuimov, A. D.; Koskin, I. P.; Frantseva, E. S.; Rybalova, T. V.; Shundrina, I. K.; Becker, C. S.; Mostovich, E. A. Synthesis, Luminescence and Charge Transport Properties of Furan/Phenylene Co-Oligomers: The Study of Conjugation Length Effect. *Org. Electron.* **2018**, *56*, 208-215.

(7) Lakowicz, J. R. Energy Transfer. In *Principles of Fluorescence Spectroscopy*; Lakowicz, J. R., Ed.; Springer US: Boston, MA, 2006; pp 443-475.

(8) Jackson, W. B.; Amer, N. M.; Boccara, A. C.; Fournier, D. Photothermal Deflection Spectroscopy and Detection. *Appl. Opt.* **1981**, *20*, 1333-1344.

(9) Goris, L.; Haenen, K.; Nesládek, M.; Wagner, P.; Vanderzande, D.; De Schepper, L.; D'haen, J.; Lutsen, L.; Manca, J. V. Absorption Phenomena in Organic Thin Films for Solar Cell Applications Investigated by Photothermal Deflection Spectroscopy. *J. Mater. Sci.* **2005**, *40*, 1413-1418.

(10) Madigan, C.; Bulović, V. Modeling of Exciton Diffusion in Amorphous Organic Thin Films. *Phys. Rev. Lett.* **2006**, *96*, 046404.

(11) Akselrod, G. M.; Prins, F.; Poulikakos, L. V.; Lee, E. M. Y.; Weidman, M. C.; Mork, A. J.; Willard, A. P.; Bulović, V.; Tisdale, W. A. Subdiffusive Exciton Transport in Quantum Dot Solids. *Nano Lett.* **2014**, *14*, 3556-3562.

(12) Hanwell, M. D.; Curtis, D. E.; Lonie, D. C.; Vandermeersch, T.; Zurek, E.; Hutchison, G. R. Avogadro: An Advanced Semantic Chemical Editor, Visualization, and Analysis Platform. *J. Cheminf.* **2012**, *4*, 17.

(13) Prutskij, T.; Percino, M. J.; Perova, T. S. Polarization Anisotropy of Photoluminescence from Triphenylamine-Based Molecular Single Crystals. *Cryst. Res. Technol.* **2013**, *48*, 1039-1043.

(14) Gallus, G.; Wolf, H. C. Excitonendiffusion in Naphthalin-Aufdampfschichten. *Zeitschrift für Naturforschung A* **1968**, *23*, 1333.

(15) Mulder, B. J. Anisotropy of Light Absorption and Exciton Diffusion in Anthracene Crystals Determined from Externally Sensitized Fluorescence. *Philips Res. Rep.* **1967**, *22*, 142.

(16) Gillus, G.; Wolf, H. C. Direct Measurement of the Diffusion Length of Singulet Excitons in Solid Phenanthrene. *Phys. Status Solidi (b)* **1966**, *16*, 277-280.

(17) Vaubel, G.; Baessler, H. Diffusion of Singlet Excitons in Tetracene Crystals. *Mol. Cryst. Liq. Cryst.* **1970**, *12*, 47-56.

(18) Lunt Richard, R.; Benziger Jay, B.; Forrest Stephen, R. Relationship between Crystalline Order and Exciton Diffusion Length in Molecular Organic Semiconductors. *Adv. Mater.* **2009**, *22*, 1233-1236.

(19) Powell, R. C.; Soos, Z. G. Singlet Exciton Energy Transfer in Organic Solids. *J. Lumin.* **1975**, *11*, 1-45.

(20) Michel-Beyerle, M. E.; Haberkorn, R.; Kinder, J.; Seidlitz, H. Direct Evidence for the Singlet-Triplet Exciton Annihilation in Anthracene Crystals. *Phys. Status Solidi (b)* **1978**, *85*, 45-49.

(21) Kalinowski, J.; Stampor, W.; Di Marco, P.; Garnier, F. Photogeneration of Charge in Solid Films of A-Sexithiophene. *Chem. Phys.* **1998**, *237*, 233-243.

(22) Lewis, A. J.; Ruseckas, A.; Gaudin, O. P. M.; Webster, G. R.; Burn, P. L.; Samuel, I. D. W. Singlet Exciton Diffusion in MEH-PPV Films Studied by Exciton–Exciton Annihilation. *Org. Electron.* **2006**, *7*, 452-456.

(23) Podzorov, V.; Pudalov, V. M.; Gershenson, M. E. Field-Effect Transistors on Rubrene Single Crystals with Parylene Gate Insulator. *Appl. Phys. Lett.* **2003**, *82*, 1739-1741.

(24) Podzorov, V. Organic Single Crystals: Addressing the Fundamentals of Organic Electronics. *MRS Bull.* **2013**, *38*, 15-24.

(25) Kazantsev, M. S.; Beloborodova, A. A.; Frantseva, E. S.; Rybalova, T. V.; Konstantinov, V. G.; Shundrina, I. K.; Paraschuk, D. Y.; Mostovich, E. A. Methyl Substituent Effect on Structure, Luminescence and Semiconducting Properties of Furan/Phenylene Co-Oligomer Single Crystals. *CrystEngComm* **2017**, *19*, 1809-1815.

(26) Glushkova, A. V.; Poimanova, E. Y.; Bruevich, V. V.; Luponosov, Y. N.; Ponomarenko, S. A.; Paraschuk, D. Y., Proc. SPIE, 2017, 10365, Organic Field-Effect Transistors XVI, 1036504.

(27) Bisri, S. Z.; Takenobu, T.; Yomogida, Y.; Shimotani, H.; Yamao, T.; Hotta, S.; Iwasa, Y. High Mobility and Luminescent Efficiency in Organic Single-Crystal Light-Emitting Transistors. *Adv. Funct. Mater.* **2009**, *19*, 1728-1735.